Sea waves impact on turbulent heat fluxes in the Barents Sea according to numerical modeling

Stanislav Myslenkov[1,2,3] Anna Shestakova[4], Dmitry Chechin[4,5]

[1]Lomonosov Moscow State University, 119991, Moscow, Russia

[2]Shirshov Institute of Oceanology RAS, 117997, Moscow, Russia

[3]Hydrometeorological Research Centre of the Russian Federation, 123242, Moscow, Russia

[4]A.M.Obukhov Institute of Atmospheric Physics RAS, 119017, Moscow, Russia

[5]Moscow Institute of Physics and Technology, 119017, Moscow, Russia

Correspondence to: Stanislav Myslenkov (stasocean@gmail.com)

Abstract. This paper investigates the impact of sea waves on turbulent heat fluxes in the Barents Sea. The COARE algorithm, meteorological data from reanalysis and wave data from the WWIII wave model results were used. The turbulent heat fluxes were calculated using the modified Charnock parameterization for the roughness length and several parameterizations, which explicitly account for the sea waves parameters. A catalog of storm wave events and a catalog of extreme cold-air outbreaks over the Barents Sea were created and used to calculate heat fluxes during extreme events.

The important role of cold-air outbreaks in the energy exchange between the Barents Sea and the atmosphere is demonstrated. A high correlation was found between the number of cold-air outbreaks days and turbulent fluxes of sensible and latent heat, as well as with the net flux of long-wave radiation averaged over the ice-free surface of the Barents Sea during a cold season.

The differences in the long-term mean values of heat fluxes calculated using different parameterizations for the roughness length are small and are on average 1-3% of the flux magnitude. Parameterizations of Taylor and Yelland and Oost et al. on average lead to an increase of the magnitude of the fluxes, and the parameterization of Drennan et al. leads to a decrease of the magnitude of the fluxes over the entire sea compared to the Charnock parameterization.

The magnitude of heat fluxes and their differences during the storm wave events exceed the mean values by a factor of 2. However, the effect of explicit accounting for the wave parameters is, on average, small and multidirectional, depending on the used parameterization for the roughness length. In the climatic aspect, it can be argued that the explicit accounting for sea waves in the calculations of heat fluxes can be neglected.

However, during the simultaneously observed storm waves and cold-air outbreaks, the sensitivity of the calculated values of fluxes to the used parameterizations increase along with the turbulent heat transfer increase. In some extreme cases, during storms and cold-air outbreaks, the difference exceeds 700 W m^{-2}.

Keywords: Barents Sea; turbulent heat flux; Charnock parameter; COARE; wind wave hindcast; cold-air outbreaks

1. Introduction

Atlantic water undergoes a significant transformation in the Barents Sea where its characteristics, such as temperature, salinity and density, change. New water masses are formed which contain different volumes of the original Atlantic water (Ivanov and Timokhov, 2019). A significant part of the heat content of Atlantic water is spent on melting ice and heating the atmosphere influencing the climatic characteristics of the region (Rahmstorf and Ganopolski, 1999). To a large extent, the heat exchange between the Barents Sea and the atmosphere is carried out by the turbulent heat flux. The Barents Sea is known to be one of the most efficient heat sinks from the ocean to the atmosphere (Simonsen and Haugan, 1996). On average, turbulent heat transfer in the Barents Sea is about 30 W/m2, according to modeling data (Arthun and Schrum 2010). However, even rough reanalysis data show that in energy active zones near the ice edge, fluxes can reach 500 W/m2 (Hakkinen and Cavalieri 1989). The latter depends on the surface roughness, which is associated with the wind wave parameters. Thus, adequate representation of surface roughness is crucial for correct estimates of the surface heat flux.

The modern models of the atmosphere and ocean commonly use the Charnock formula (Charnock, 1955) as a parameterization of the aerodynamic roughness length over the water. The Charnock relationship represents a quadratic dependence of the roughness length on the friction velocity. The Charnock parameter as constant, which represents the proportionality coefficient between the roughness length and the square of friction velocity, used in the most frequently models and reanalyses (for example, in NCEP/NCAR, NCEP/CFSR, MERRA reanalyses). However, numerous studies of roughness behavior in different conditions according to observational data (e.g. Oost et al. 2002, Mahrt et al. 2003) showed that the Charnock parameter (coefficient) is not constant, especially in conditions of high wind speed and high waves. The Charnock formula is applicable when the wave state is in equilibrium with wind forcing, and does not take into account the age of the waves and such effects as wave breaking and spray formation.

Thereby, several parametrizations were proposed that explicitly or implicitly take into account the influence of such wave parameters as wave height, wave length and period on the sea surface roughness.

In the most simple modification of the Charnock formulation the Charnock parameter is set as a piecewise constant or a linear function of wind speed in order to fit the observations. In other parametrizations, the Charnock parameter explicitly depends on the wind wave parameters, usually the wave steepness (Taylor and Yelland 2001) and wave the age (Jones and Toba 2001, Oost et al. 2002, Drennan et al. 2003). More complex parameterizations are based on the relation between the roughness length and the wave momentum flux (Janssen 1991) and are typically used in coupled wave-atmosphere models, including ECMWF operational analysis and reanalyses (ECMWF 2007). Intercomparisons of different roughness parametrizations, including Taylor and Yelland (2001), Oost et al. (2002) and Drennan et al. (2003) parametrizations, did not reveal the best of them (Pan et al. 2008, Charles and Hemer 2013, Shimura et al. 2017, Kim et al. 2018, Prakash et al. 2019). Some studies have shown that Oost et al. parametrization overestimates the roughness of the sea surface in comparison with other schemes (Pan et al. 2008, Kim et al. 2018), and Drennan et al. parametrization usually gives a lower roughness (Charles and Hemer 2013).

The choice of roughness length parameterization affects primarily the momentum flux and turbulent heat transfer. The sensible and latent heat fluxes are calculated using the roughness length for temperature and specific humidity, respectively. The ratio of the roughness lengths for scalars and momentum is typically parameterized as function of the Reynolds roughness number (Brutsaert 1982, Zilitinkevich et al. 2001, Renfrew et al. 2002, Brunke et al . 2011).

The turbulent heat transfer in most reanalyses is parameterized using bulk formulae. The choice of the parameterization for the roughness length for temperature and humidity, parameterization of the Charnock parameter, and of the universal functions describing the dependence of the transfer coefficients on the surface layer stratification

(Renfrew et al. 2002, Brunke et al. 2011). A list of the parameterizations used in the different reanalyses is given in the Appendix by Brunke et al. (2011).

The use of certain parameterization can significantly affect the value of the calculated heat and momentum fluxes. For instance, the difference in the total turbulent heat flux between the two most commonly used algorithms, NCAR (Large and Yeager, 2009) and COARE (Coupled Ocean Atmosphere Response Experiment) (Fairall et al. 1996), is 13 W/m^2 on average throughout the globe and reaches 15-20% of the flux magnitude in mid-latitudes and subpolar regions (Brodeau et al. 2017). Typical values of the average difference of turbulent fluxes produced by different algorithms and the observational data amount to 5-15 W/m^2. Unambiguously "the best set of parameterizations" of the roughness length and universal functions for calculating heat and momentum fluxes does not exist (Brunke et al. 2011;, Charles and Hemer 2013). Nevertheless, the widely used COARE algorithm (Fairall et al. 1996, Fairall et al. 2003), which is also embedded in satellite flux calculation algorithms, is considered the most reliable for calculating turbulent fluxes. Satellite products such as J-OFURO, HOAPS, and OAFlux (joint satellite and simulation product), use algorithms very similar to COARE (Brunke et al. 2011, Yu et al. 2011). The COARE algorithm offers a choice of Taylor and Yelland (2001) and Oost et al. (2002) roughness length parameterizations, which explicitly take into account the wind wave parameters.

Roughness length dependency on wind wave parameters is expected to have regional differences depending on the local features of the wave regime. According to studies (Wind and Wave…, 2003; Stopa et al., 2016; Liu Q. et al., 2016), a strong winds and high waves observed in the Barents Sea most of the year. The duration of periods in which the wind speed does not exceed 15 m/s in the winter months averages only 3–6 days. The mean wave height (probability of exceedance 50%) with a frequency of occurrence of 1 time per year is 6.1 m, and the maximum wave height (probability of exceedance 0.1%) is more than 19 m (Wind and Wave…, 2003). Such values indicate the high frequency of occurrence of extreme waves. The average significant wave heights of in the Barents Sea is 1.8–2.2 m for the central part of the Barents Sea (Myslenkov et al., 2019). The maximum of significant wave heights reaches 12–14 m in the central part of the Barents Sea. The storms with significant wave heights of more than 4 m are observed on average 70–80 times a year, with significant wave heights more than 5 m - 40–60 times a year. The interannual variability of the recurrence of storm waves is very large (for different years the number of cases can vary by a factor of 2–3) (Myslenkov et al., 2018, 2019).

Moreover, the wave climate of the Barents Sea is characterized by a significant influence of swell coming from the North Atlantic. Based on numerical experiments (Myslenkov et al., 2015), it was shown that the height of swell can reach 5 m with a period of 15-18 sec. The effect of swell is not taken into account in the Charnock relationship explicitly, which can cause errors in the calculated values of the roughness length and turbulent fluxes.

In addition to wind speed, the difference of temperature and specific humidity between the sea surface and air also affects the magnitude of turbulent heat fluxes over the sea. These differences reach particularly large values during the so-called cold-air outbreaks (CAOs). CAOs represent the advection of a dry and cold air mass onto the open sea originating from the Central Arctic or from the cold continents (Pithan et al., 2018). The temperature difference between water and air during CAOs can exceed 30 °C near the marginal sea ice zone, and the maximum values of the total turbulent heat flux can exceed 600 W/m^2 (Brümmer, 1996). As the air mass warms and moistens with increasing distance from the ice edge, the total heat flux decreases. The horizontal scale of the air mass transformation is about 500-1000 km for typical CAOs (Chechin and Lüpkes, 2017). Thus, large areas of the non-freezing seas, such as the Barents Sea, are subject to intense heat loss. The heat loss due to CAOs can reach up to 60% over the Greenland and Iceland Seas (Papritz and Spengler, 2017), although the specific value depends on the criteria used for the identification of CAOs. To our knowledge, no systematic study of the CAOs role in the air-sea heat exchange exists for the Barents Sea, although the importance of CAOs has been stressed earlier (Smedsrud et al., 2013).

Furthermore, CAOs create favorable conditions for enhancing wind speed over water, which leads to further intensification of the energy exchange. The wind speed increase is primarily associated with the formation of large horizontal temperature gradients and strong baroclinicity. This can lead to the intensification of cyclones and mesocyclones (Kolstad, 2015), formation of jets and wind shear along the lower tropospheric fronts (Grønas and Skeie, 1999), convergence lines (Savijärvi, 2012), and low-level jets (Brümmer 1996; Chechin et al., 2013; Chechin and Lüpkes, 2019). Although the highest wind speeds over the Barents Sea have the orographic origin (e.g., the Novaya Zemlya Bora (Moore, 2013)), it was shown (Kolstad, 2015) that in cyclones, the wind speed reaches its maximum value when intense cold advection takes place in their rear part. In addition, intense turbulent exchange in the convective boundary layer effectively transports momentum down to the lower atmospheric layer increasing the near-surface wind speed (Chechin et al., 2015).

In this paper, we consider the influence of sea waves on turbulent heat fluxes in the Barents Sea. Heat fluxes were calculated using the COARE 3.0 algorithm and NCEP/CFSR reanalysis data with the Charnock roughness length parameterization and parameterizations explicitly taking into account the parameters of sea waves - Taylor and Yelland (2001), Oost et al. (2002) and Drennan et al. (2003). The results were verified by the ship measurements of turbulent heat fluxes obtained during the NABOS (Nansen and Amundsen Basins Observational System) campaigns in different years. The wind wave parameters were obtained from the WaveWatchIII (WWIII) wave model. Special attention is paid to the cases of intense storms and cold-air outbreaks events, when the expected difference between calculations with different roughness parameterizations is the largest.

2. Data and Methods

2.1 Wave modeling

The wave characteristics in the Barents Sea were computed using the spectral wave model WaveWatchIII (WWIII) version 4.18. The WWIII model is a development of the WAM model with regard to the functions of the source and the nonlinear interaction (Tolman, 2014). This model is based on a numerical solution of the equation of the spectral wave energy balance

$$\frac{\partial E(\omega, \theta, \vec{x}, t)}{\partial t} + \vec{V}(\omega, \theta)\nabla E = S(\omega, \theta, \vec{x}, t), \quad (1)$$

where ω and θ are the frequency and the propagation direction of the spectral component of the wave energy; $E(\omega, \theta, \vec{x}, t)$ is the two-dimensional spectrum of the wave energy at a point with vector coordinate $\vec{x}$ at time point t; $\vec{V}(\omega, \theta)$ is the group velocity of the spectral components; $S(\omega, \theta, \vec{x}, t)$ is a function that describes the wave energy sources and sinks, i.e., the transfer of the energy from the wind to the waves, nonlinear wave interactions, dissipation of the energy through collapse of the crests at a great depth and in the coastal zone, friction against the bottom and ice, wave scattering by ground relief forms, and reflection from the coastline and floating objects. The energy balance equation is integrated using finite-difference schemes by the geographic grid and the spectrum of wave parameters.

In this work, the computations were made using the ST1 scheme (Tolman, 2014). To account for the nonlinear interactions of the waves, the Discrete Interaction Approximation (DIA) model (Hasselmann and

Hasselmann, 1985) was used, which is a standard approximation for calculation of nonlinear interactions in all modern wave models.

To take into account ice effects on the wave development, the IC0 scheme was used, where the grid point is considered as ice-covered if the ice concentration was larger than 0.25. Thus, the exponential attenuation of wave energy adjusted for the sea ice concentration at a given point was added.

In the shallow water, the increase in wave height as waves approach the shore and the related wave breaking after waves reach the critical value of steepness were taken into consideration. The whitecapping effect taken into account in the ST1 scheme. The standard JONSWAP scheme was used to take the bottom friction into account. The spectral resolution of the model is 36 directions (Dq = 10°), the frequency range consists of 36 intervals (from 0.03 to 0.843 Hz).

The calculations were performed using the original unstructured grid, which is based on the bottom topography data from ETOPO1 database and detailed nautical charts (Figure 1). This unstructured grid consists of 16792 nodes; the spatial resolution varies from 15 km for the open part of the Barents Sea to 500 m for the coastal regions. The computational domain of the model covers the Barents and the Kara Seas and the entire northern part of the Atlantic Ocean (Figure 1). Previously, this grid was successfully used for wave modeling (Myslenkov et al., 2018; Myslenkov et al., 2019). The need to take into account the swell propagating from Atlantic ocean when calculating the height of significant waves in the Barents Sea was clearly shown in the previous work of the authors (Myslenkov et al., 2015).

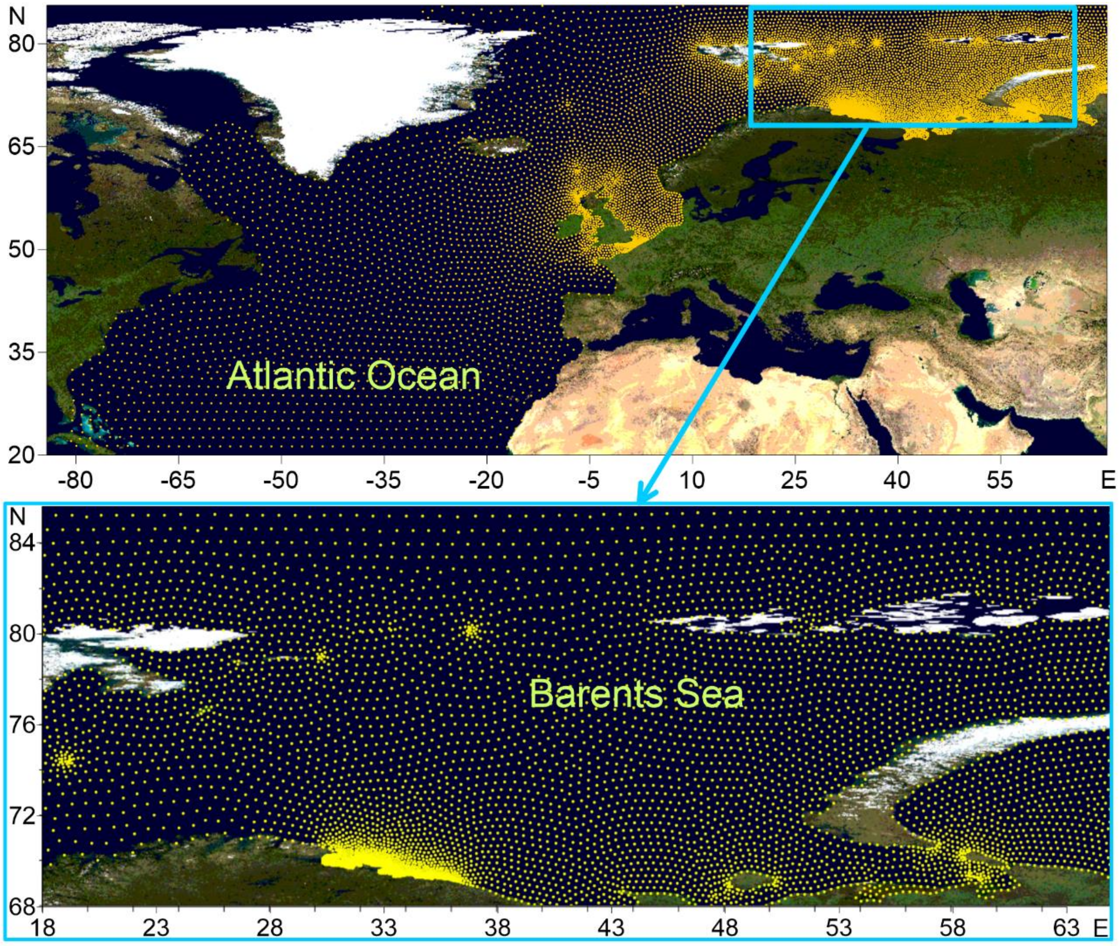

Figure 1. The computational unstructured grid for the Atlantic Ocean and the Barents Sea. The base map is the Blue Marble which obtained by connecting to the WMS demo server in the Surfer Golden Software program.

The general time step for the integration of the full wave equation was 15 minutes, the time step for the integration of functions of sources and sinks of wave energy was 60 s, the time step for the spectral energy transfer and for satisfying the Courant–Friedrichs–Lewy condition was 450 s. This choice is dictated by the configuration of the computational grid: the maximum and minimum distances between the nodes and a large latitudinal extent.

The 10-m wind from the NCEP/CFSR reanalysis (Saha et al., 2010) for the period of 1979 to 2010 with the spatial resolution of ~0.3° was used as the forcing. Data of NCEP/CFSv2 reanalysis (Saha et al., 2014) with the resolution of ~0.2° and with the time step of 1 hour were used for the period of 2011 to 2017.

The wave model quality assessments based on Cryosat satellite data for period 2010-2017 (data collected from IMOS satellite database (Ribal and Young, 2019)). A comparison of the modeled and satellite SWH is shown on Figure 2. The model calculations provides the R (correlation coefficient) is 0.88, the BIAS is -0.04 m, and the RMSE is 0.53 m. The Scatter Index is 0.28. The results of quality assessments based on the satellite data is similar to other assessments (Li et al., 2019, Stopa et al., 2016).

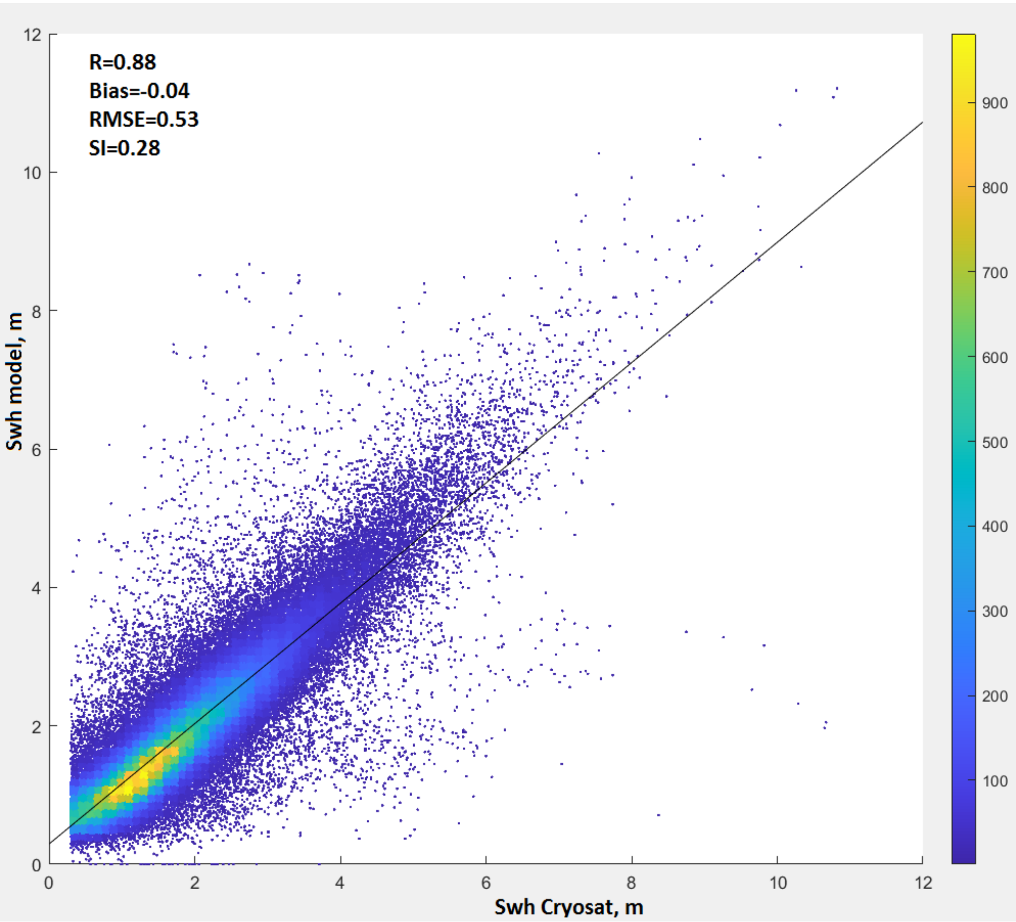

Figure 2. Scatter diagram of model SWH and satellite data.

In this paper, we used the output results of the wave model with time step 3 hours from 1979 to 2017 for each node of the unstructured grid.

Based on the wave model results, a study of storm activity was carried out according to the POT (Peak Over Threshold) method which used successfully earlier in (Myslenkov et al., 2019). For each year in the Barents Sea, the number of storm surges with different significant wave heights from 5 to 8 m was calculated. The event is counted as the storm with wave height > 5 m if at least in one node in the study area the wave height exceeds the threshold of 5 m This event continues until the wave height at all nodes becomes less than the threshold. To eliminate possible errors, at least 9 hours should pass between two storm events. Using the described procedure, a catalog of storm days was compiled when the significant wave heights of more than 5 m were observed. A total of 1964 days were identified for the period 1979-2017.

2.2 COARE algorithm and parameterizing the roughness parameter

Turbulent heat fluxes were calculated using the COARE algorithm (Fairall et al., 1996), based on the LKB model (Liu et al., 1979). Bulk formulae for the momentum and scalar fluxes have the general form:

$$w'x' = c_x^{1/2} c_d^{1/2} S \Delta X = C_x S \Delta X, \qquad (2)$$

where w' is the fluctuations of vertical wind, x can be a horizontal wind components u, v, temperature or specific humidity, c_x – transfer coefficients for x, c_d – transfer coefficient for momentum, C_x – total transfer coefficient, ΔX – the difference the mean x at a height equal to the roughness length and at a certain height (10 m) in the atmospheric surface layer (Fairall et al., 2003). S – mean wind speed with gusts U_g:

$$S = \sqrt{U^2 + V^2 + U_g^2}$$

The default value of U_g is 0.5 m/s in the COARE algorithm. Transfer coefficients depend on the roughness length and dimensionless universal functions. The form of universal functions in the COARE algorithm is set in accordance with (Beljaars and Holtslag, 1991) for stable stratification; the so-called Kansas functions (Kaimal et al., 1972) are used for unstable stratification; functions from Fairall et al. (1996) and Grachev et al. (2000) are used for very unstable stratification. For the roughness length, several parameterizations are available in the COARE algorithm. The parameterization of Charnock (Charnock, 1955) implies dependence of roughness on the friction velocity u_*:

$$z_0 = \frac{\alpha u_*^2}{g} + \frac{0.11a}{u_*} \qquad (3)$$

where α – Charnock parameter, g – gravity acceleration, a – kinematic viscosity coefficient (Andreas, 1989). Equation (3) is the modified Charnock formula (Smith, 1988), in which the second term on the right side describes the roughness over an aerodynamically smooth surface (i.e., in weak winds). The Charnock coefficient is set piecewise constant in strong and weak winds and linearly dependent on 10-m wind speed in moderate winds:

$$\begin{cases} 0.011, & S < 10 \ m/s \\ 0.011 + \dfrac{0.007(S-10)}{8}, & 10\ m/s < S < 18\ m/s \\ 0.018, & S > 18\ m/s \end{cases}$$

In the parameterization of Taylor and Yelland (2001) (hereafter - T1), the roughness length is related to the wave steepness (H_s/L_p):

$$z_0 = H_s a_1 \left(\frac{H_s}{L_p}\right)^{b_1} + \frac{0.11a}{u_*}, \quad a_1 = 1200, \quad b_1 = 4.5 \qquad (4)$$

where H_s – significant wave height, L_p – spectral peak wavelength.

The parameterization of Oost et al. (2002) (hereafter - O2) implies the dependence of the roughness length on the spectral peak wavelength L_p and inverse wave age (u_*/c_p):

$$z_0 = L_p a_2 \left(\frac{u_*}{c_p}\right)^{b_2} + \frac{0.11a}{u_*}, \quad a_2 = 50/2\pi, \quad b_2 = 4.5 \qquad (5)$$

Here c_p –phase wave speed associated with spectral peak, which is expressed through the wave length as $c_p = \sqrt{L_p g / 2\pi}$.

Finally, we included the parametrization of Drennan et al. (2003) (hereafter - D3) in the COARE algorithm. D3 parameterization consists in the dependence of the roughness length on the wave height and inverse wave age:

$$z_0 = H_s a_3 (\frac{u_*}{c_p})^{b_3} + \frac{0.11a}{u_*}, \quad a_3 = 3.35, \quad b_3 = 3.4 \qquad (6)$$

Thus, the main components of the algorithm are the equation (2), formulae for calculating transfer coefficients based on the Monin-Obukhov similarity theory, and formulae (3-6) for the roughness length. Thus, in general, the COARE algorithm is similar to corresponding algorithms in most atmospheric models.

Using the COARE algorithm, we calculated turbulent sensible and latent heat fluxes in the Barents Sea from 1979 to 2017. Mean fluxes were calculated for long-term period and for periods of cold-air outbreaks and storm wave events. Since the scatter index of our modeled significant wave heights is 0.28 (or 28%), then probably this value can lead to mean errors ~4-5% in the calculated heat flux values.

2.3 Input data for the COARE algorithm

Input data for the COARE algorithm are: wind vector, air temperature, sea surface temperature (SST), air humidity, incoming short-wave and long-wave radiation, precipitation intensity, sea wave height and period. NCEP/CFSR and CFSv2 (Saha et al., 2010, 2014) reanalysis with temporal resolution of 6 hours and total period 1979-2017 were used as atmospheric data input for the COARE algorithm. CFSv2 reanalysis data for the period 2011-2017 (with a slightly better spatial resolution than CFSR, were interpolated from the ~0.2˚ grid to ~0.3˚ grid to match the CFSR resolution. The wind speed was used at 10 m height, air temperature and humidity were used at 2 m height. Reanalysis data are also available at isobaric levels, the lower of which is 1000 hPa. However, we preferred to take diagnostic variables at heights of 2 and 10 m for several reasons. Firstly, the height of the isobaric levels varies greatly and the lower available level may be at a high height (above the boundary layer). Secondly, data at vertical levels are available on a much coarser grid (0.5 °). For instance, Arthun and Schrum (2010) also used diagnostic variables at standard levels from the NCEP-NCAR reanalysis to calculate turbulent fluxes in the ocean model. The surface pressure and the inversion height (boundary layer height), which are usually set constant in the COARE algorithm, were set from the CFSR reanalysis (at each moment of time and at each grid point).

2.4 Ship observations

We used ship observations in the Barents Sea from the NABOS expeditions in 2005, 2007, 2013, and 2015 to verify turbulent heat fluxes calculated using the COARE algorithm. All expeditions took place in a period from August to October. Ship-borne fluxes were calculated using the eddy-covariance method (the left side of equation (2)) based on high-frequency measurements of temperature and the three wind components using Gill and Metek sonic anemometers (Ivanov et al., 2019; Varentsov et al., 2016). The averaging period for the covariance calculations was 10 min. For all wind measurements, a correction was made for the movement of the ship. A detailed description of the location of the instruments and methods of filtering data and calculating fluxes is available at https://uaf-iarc.org/nabos-cruises/. For verification, the calculated values of heat fluxes were bilinearly interpolated (using 4 surrounding points) from the CFSR reanalysis grid to the observation points.

2.5. Identification of CAOs

The so-called «CAO index» is frequently used for CAO identification. It was first defined (Kolstad and Bracegirdle, 2008; Kolstad et al., 2009) as the potential temperature difference between the ocean surface and the 700 hPa height normalized by the pressure difference at the same heights. The authors used the value of the 90th percentile of the CAO index to estimate the strength and frequency of occurrence of CAOs. Other investigators (e.g., Fletcher et al., 2016) used the non-normalized potential temperature difference between the surface and the 800hPa height. As metrics to study the frequency and strength of CAOs they evaluated the frequency of occurrence of the positive values of the CAO index, as well as the value of the 95th percentile of the CAO index during the winter months.

Here, we define the CAO index I_{cao} as the daily potential temperature difference between the ocean surface and the 700 hPa height. For each day, I_{cao} was averaged over the ice-free part of the Barents sea. Figure 3 shows the obtained I_{cao} values for the period 1979-2018. Solid curve on Figure 3 consists of the multiyear-averaged values $\overline{I_{CAO}}$ obtained by 1) averaging I_{cao} over a 30-day period centered on the given day and 2) averaging the obtained values over the years. Similarly, the standard deviation σ_I of I_{cao} was obtained.

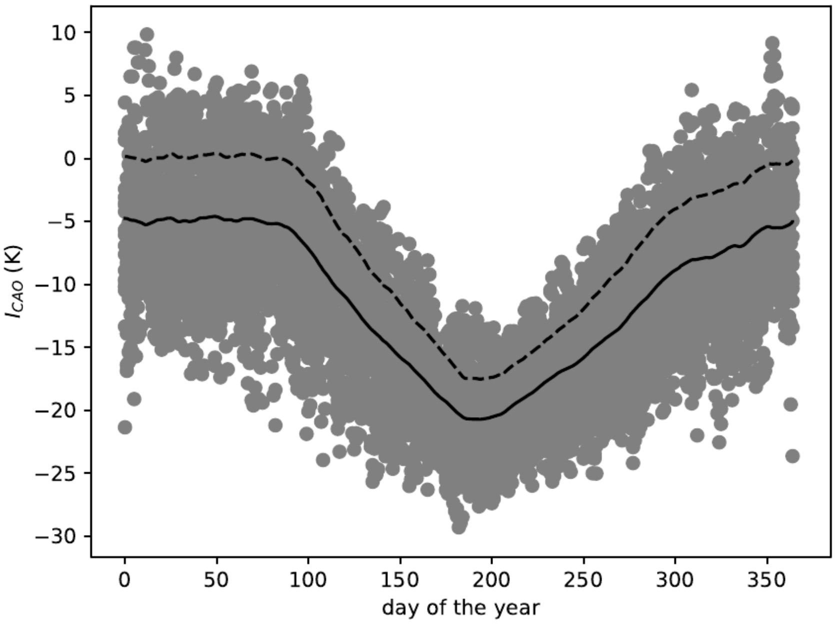

Figure 3. Cold-air outbreak index I_{cao} for the period 1997-2017. Solid curve represents the 30-day running multiyear mean values $\overline{I_{CAO}}$. Extreme CAOs correspond to points above the dashed curve which is the sum $\overline{I_{CAO}}$ + σ_I where the latter is the 30-day running multiyear standard deviation of I_{cao}.

The dashed curve in Figure 3 represents the threshold value $\overline{I_{CAO}} + \sigma_I$ which we use as a criteria for CAO identification, namely

$$I_{CAO} > \overline{I_{CAO}} + \sigma_I \qquad (7)$$

According to the criteria (7), we identify CAOs as those cases when I_{cao} values are above the dashed curve in Figure 3. A similar procedure was used in other studies (e.g., Wheeler et al., 2011) to identify continental CAOs where authors used simply the air temperature at 2 m height instead of I_{cao}.

Figure 3 shows that the largest values of I_{cao} are observed in a period from the second half of December until the end of March when the coldest air advection occurs over the Barents Sea. It is interesting to note that in winter the criteria (7) is almost identical to simply $I_{cao} > 0$. The latter serves as a measure of the dry hydrostatic stability of the layer between the ocean surface and the 700 hPa surface. Thus, positive values of I_{cao} indicate conditions favorable for the mixed-layer development to the heights over 700 hPa. During strong background advection mixed-layer can reach such heights only at a significant distance from the ice edge (Chechin and Lüpkes, 2017).

3. Results

3.1 Wave climate and storm activity

First, we consider the main features of wave conditions and wave climate in the Barents Sea, which directly affect the processes of heat exchange in the ocean-atmosphere system. In Figure 4 the average significant wave heights for the entire simulation period from 1979 to 2017 is shown. The highest average wave heights are found in the western part of the sea. Here we can expect the greatest influence of sea waves on heat fluxes. In the north, due to the presence of ice, the average wave heights do not exceed 1 m.

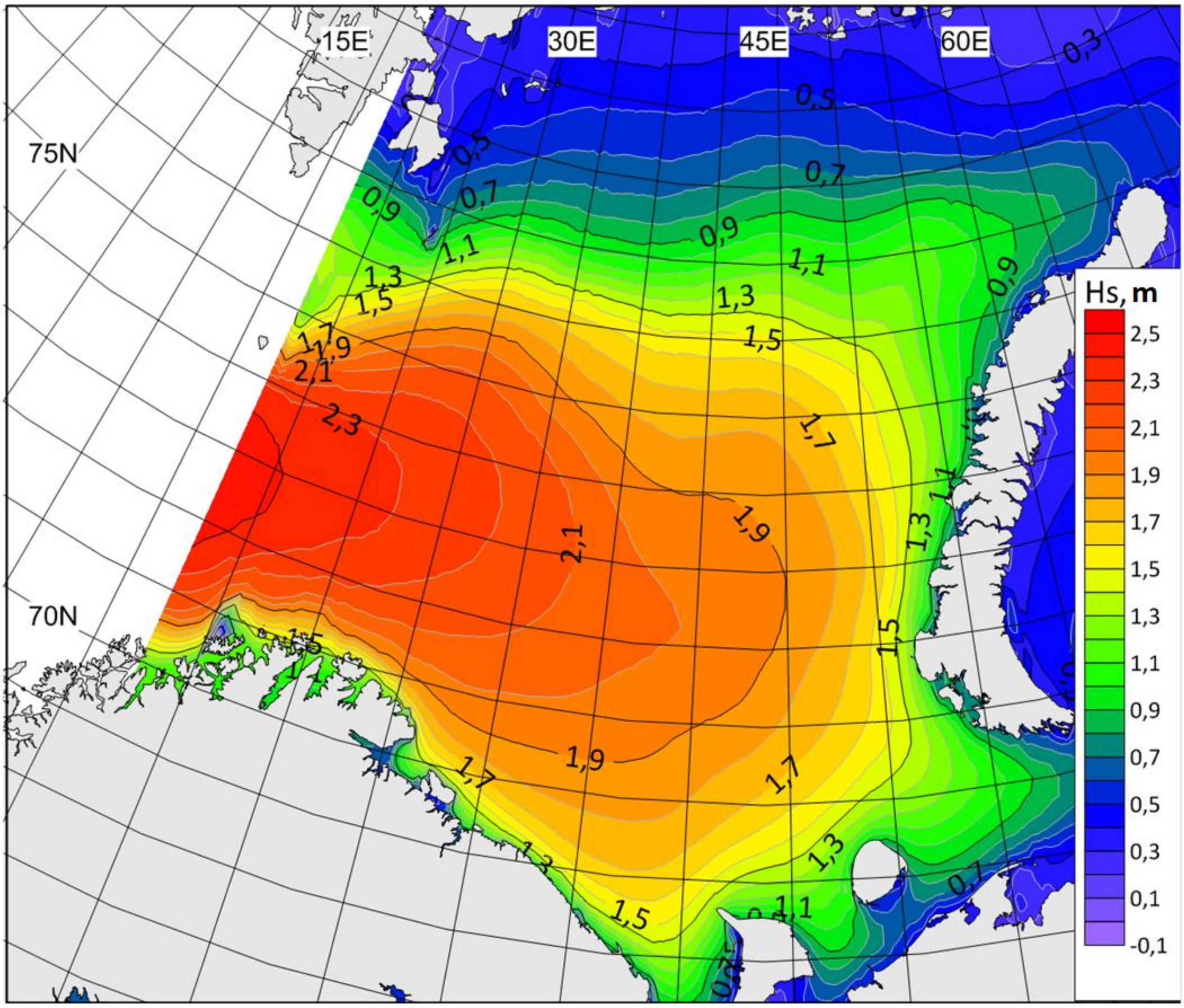

Figure 4. Long-term average significant wave height in the Barents Sea based on the WWIII simulation results for the all period 1979-2017.

Also, an equally important parameter is the wavelength, which is used in the parametrizations O2 and D3. In Figure 5 the mean long-term spectral peak wavelength is shown. The wavelengths 80-100 m are observed in the central and western parts of the Barents Sea. The results on the average wave height and wavelength in general are consistent with similar works by other authors (Semedo et al., 2011; Stopa et al., 2016). Estimates of storm activity based on such long-term analysis are relatively rare and their detailed analysis would require an additional research.

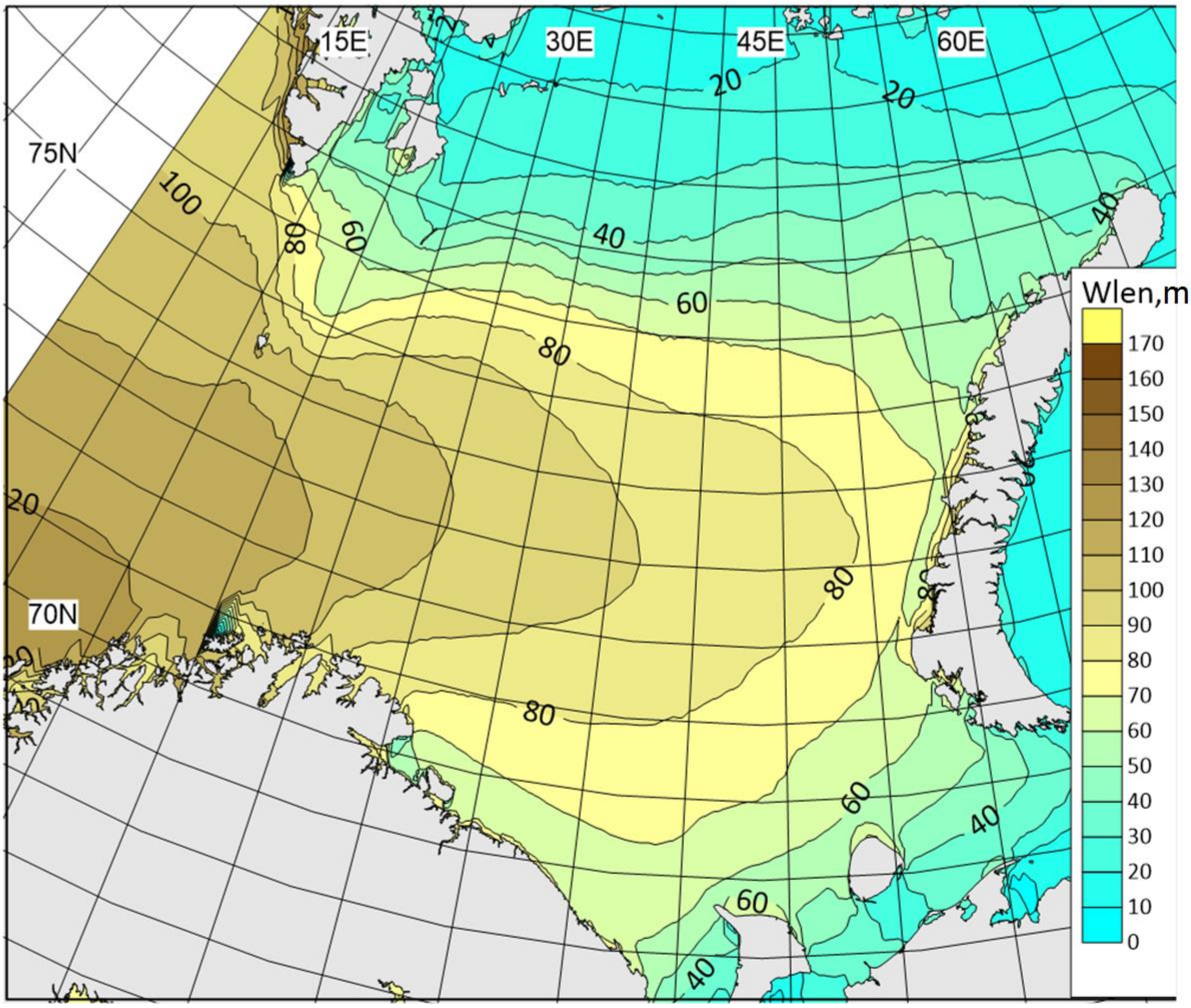

Figure 5. Long-term average long-term spectral peak wavelength in the Barents Sea based on the WWIII simulation results for the all period 1979-2017.

The Barents Sea is characterized by a high frequency of storm wave events, which provide a long swell in the extinction stage (i.e., “old seas”) and limit the applicability of the Charnock formula. As shown in (Myslenkov et al., 2018), the number of storms per year in the Barents Sea can differ significantly. Figure 6 shows the number of storms calculated according to the wave model results with wave heights of more than 5 m and more than 7 m (identified as described in the Section 2.1). During the period from 1979 to 2017, several maxima of storm activity were observed, for example, in 1989-1991 and in 2011. Especially for these periods, the calculated heat fluxes are expected to be sensitive to the used of parameterizations of the roughness length (see Section 3.5).

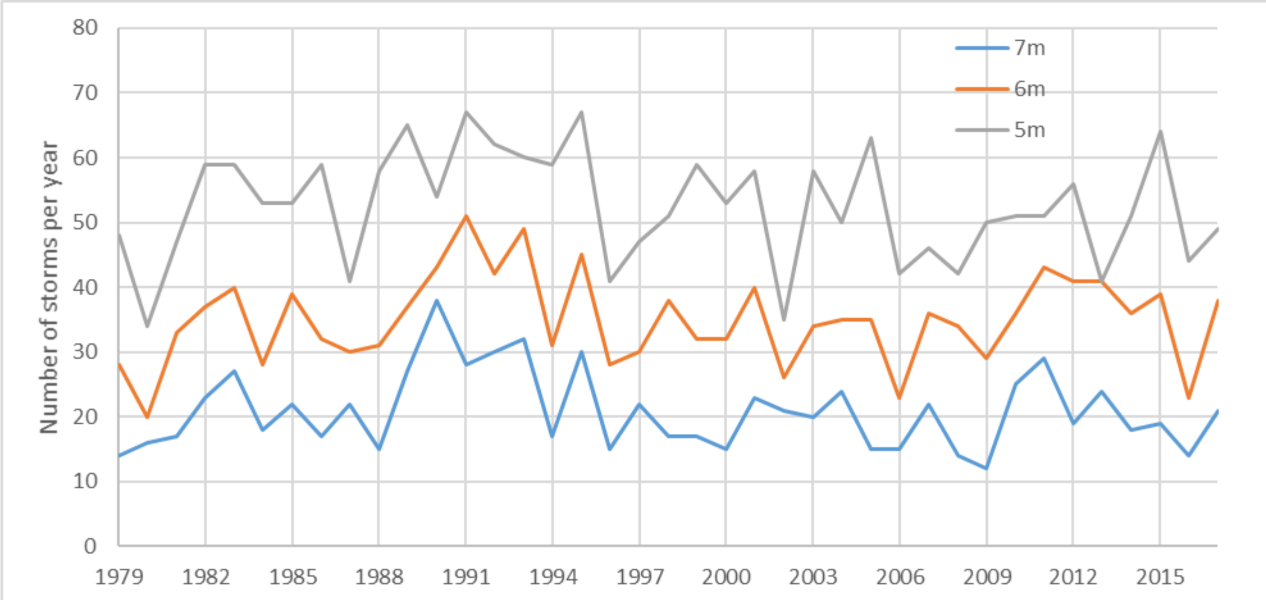

Figure 6. The number of storms with a significant wave height of more than 5, 6 and 7 m according to the WWIII simulation results for the period 1979-2017.

3.2 CAOs frequency of occurrence

Figure 7 shows the timeseries of the number of days with extreme CAOs selected using formula (7) for each cold period (November-April) of 1979-2018. On average, CAOs are observed in 16.4 % days. However, the interannual variability of the frequency of occurrence of CAOs is large. Namely, the interannual standard deviation of the number of CAO days amounts to 12 days. Thereby, the number of CAO days per cold season varies from 6 in 2011-2012 to 56 in 1980-1981.

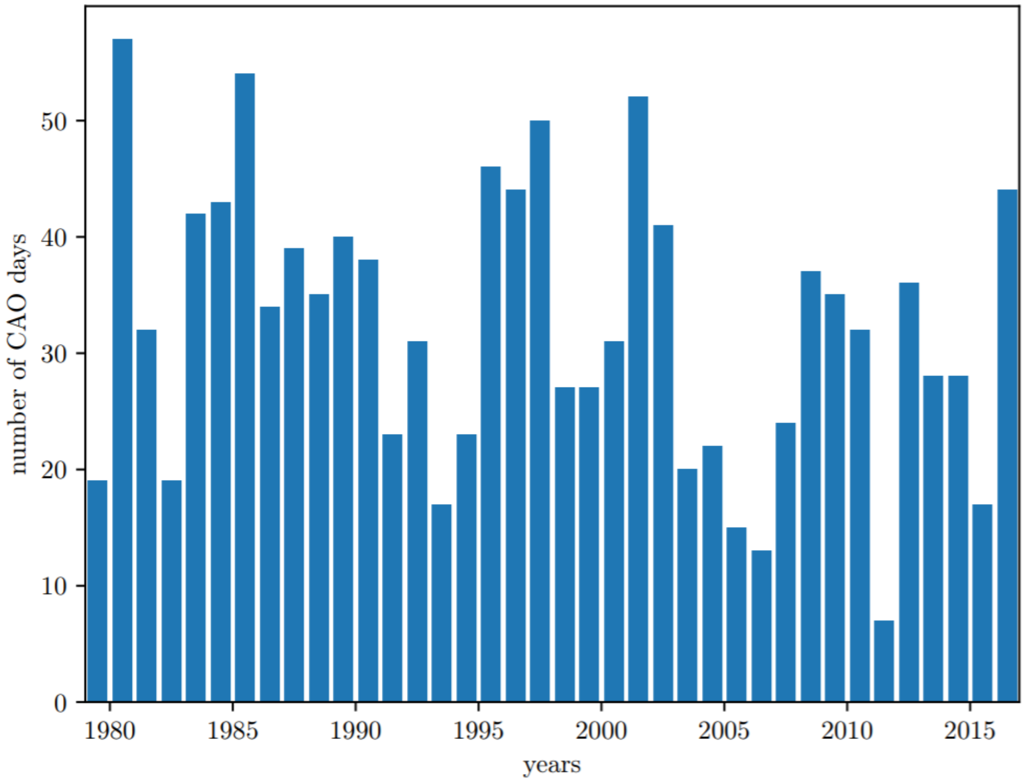

Figure 7. The number of days with CAOs over the Barents Sea selected using formula (7) for each cold season in 1979-2018.

The frequency of occurrence of CAOs over the Barents Sea is governed by the variability of the largescale patterns of atmospheric circulation. To the largest extent, the frequency of CAOs is correlated with the so-called «Barents Oscillation» (Skeie et al., 2000; Wu et al. 2006; Kolstad et al., 2009). The latter is the mode of variability of the sea-level pressure field represented by a dipole with high pressure over Greenland and Iceland and low pressure over the northern part of the European part of Russia. Such pressure field promotes intense cold-air advection over the Barents Sea from the north. Moreover, there is a negative correlation between the North Atlantic Oscillation index and CAOs frequency of occurrence (Kolstad et al., 2009). Such a correlation is particularly strong for easterly CAOs, which is obviously associated with the reduced strength of the westerlies.

A slight negative trend of the CAO days is seen in Figure 7. To a large extent, it can be explained by an increase of the mean CAO index values over the Barents Sea. Such an increase can be associated either with a higher air temperature over the Arctic in winter, i.e. CAOs become less severe, or with a decrease of the frequency of synoptic patterns favorable for CAOs (Papritz and Grams, 2018). A negative trend of the CAO index values over the Barents and Kara seas was also obtained by Narizhnaya et al. (2020) based on the ERA Interim data for the 1979-2018 period. They found an increase of the number of weak and moderate CAOs and a decrease of the number of strong CAOs.

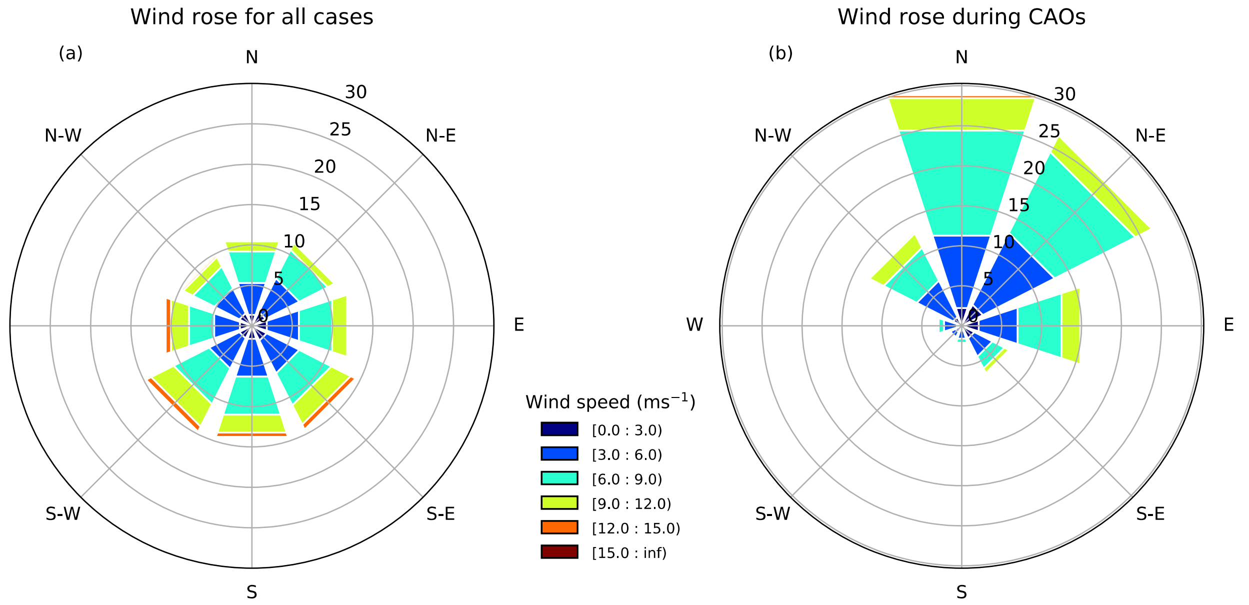

Figure 8. Frequency of occurrence of daily 10 m wind speed and direction, averaged over the ice-free part of the Barents Sea for the period November-April 1979-2018 for all cases (a) and cold-air outbreaks (b).

The frequency of CAOs with easterly wind over the Barents Sea is significant and represent up to 16% of all CAOs (Figure 8b). During CAOs, the highest frequency of occurrence have northerly (30%) and north-easterly (27%) winds. The wind rose in CAOs differs from the wind rose in all cases during the cold season (Figure 8a). In particular, the prevailing wind direction over the Barents sea in winter is from the south. Moreover, the winds having southerly and westerly components are the strongest.

The CAOs role in the heat exchange between the Barents Sea and the atmosphere is demonstrated by Figure 9. The latter shows the turbulent fluxes of sensible and latent heat, H and LE, respectively, the net longwave radiative flux LW_{net}, and the total heat flux $F_{total} = H + LE + LW_{net}$ averaged over the November-April period over the ice-free part of the Barents Sea as functions of the number of CAO days during the same period. Clearly, there is a strong dependency of the Barents Sea on the number of CAO days. The highest correlation coefficients are obtained for LW_{net}, F_{total} and H amount to 0.86, 0.85 and 0.84, respectively. A smaller correlation coefficient of 0.78 is obtained for LE. Also, the coefficients of linear regression shown in Figure 9 demonstrate that F_{total} has the strongest dependency on the number of CAO days. From all terms of the surface heat balance, the sensible heat flux H is most sensitive to the number of CAO days. All the three considered components of the surface heat balance (H, LE and LW_{net}) manifest heat loss from the sea surface to the atmosphere and are of comparable magnitude of about 70 Wm^{-2} on average.

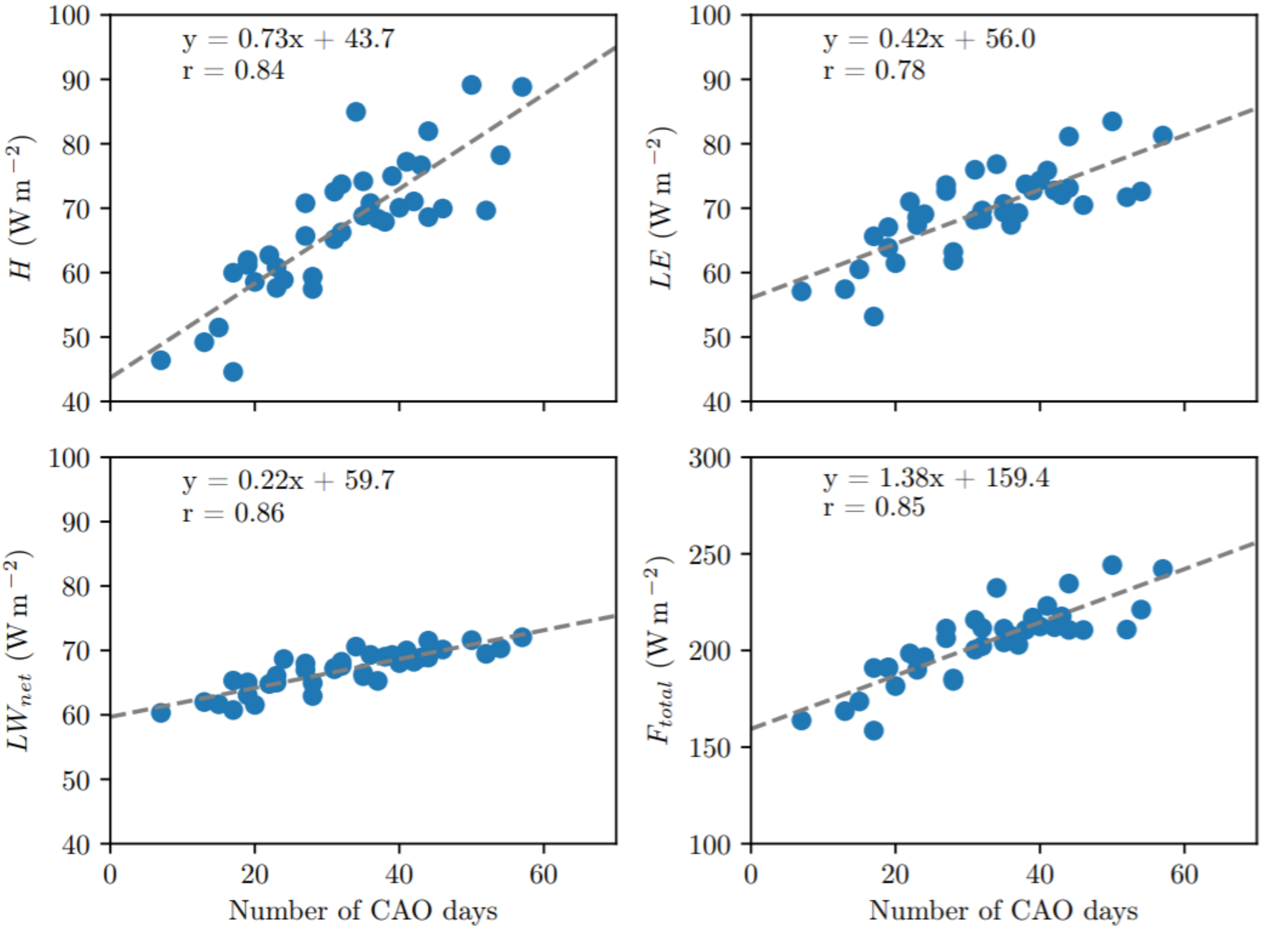

Figure 9. Turbulent fluxes of sensible and latent heat, H и LE respectively, net longwave radiative flux LW_{net} and the total heat flux $F_{total} = H + LE + LW_{net}$ averaged over the cold season (November-April) and over the ice-free part of the Barents Sea as function of number of CAO days during the same period for 1979-2018. Dashed line shows the linear regression line, whose equation is given at each plot, as well as the correlation coefficient *r*.

We stress that the values of fluxes shown in Figure 9 are averaged over the ice-free part of the Barents Sea. It is important to keep in mind that there is a large interannual variability of the area of sea ice cover in the Barents Sea. This is another important factor, along with the number of CAO days, influencing the heat loss.

One might also expect that the ice edge retreat further north leads to a larger fetch over which the cold air mass is advected. This would result in a higher air temperature over the Barents Sea which can locally decrease the surface heat flux (Pope et al., 2020). However, this would lead to an increase of the total heat loss at the surface of the Barents Sea which is proportional to the open water area. Since the sensible heat flux maximum during CAOs is located near the ice edge, the maximal heat loss location would also shift further north. This might have implications for the so-called “atlantification” in the northeastern part of the Barents Sea (e.g., Barton et al., 2018).

3.3 Verification of the COARE algorithm by the ship observations

Figure 10 shows the comparison of sensible and latent heat fluxes from shipborne observations and calculated using different roughness parameterizations, namely Charnock, 1955 (C55), Taylor and Yelland, 2001 (T1), Oost et al., 2002 (O2) and Drennan et al., 2003 (D3). Left side of Figure 10 presents calculations made on the basis of reanalysis, interpolated to cruise track, while right side of the figure presents calculations from shipborne observations of meteorological parameters and radiative fluxes (available only in 2013-2015).

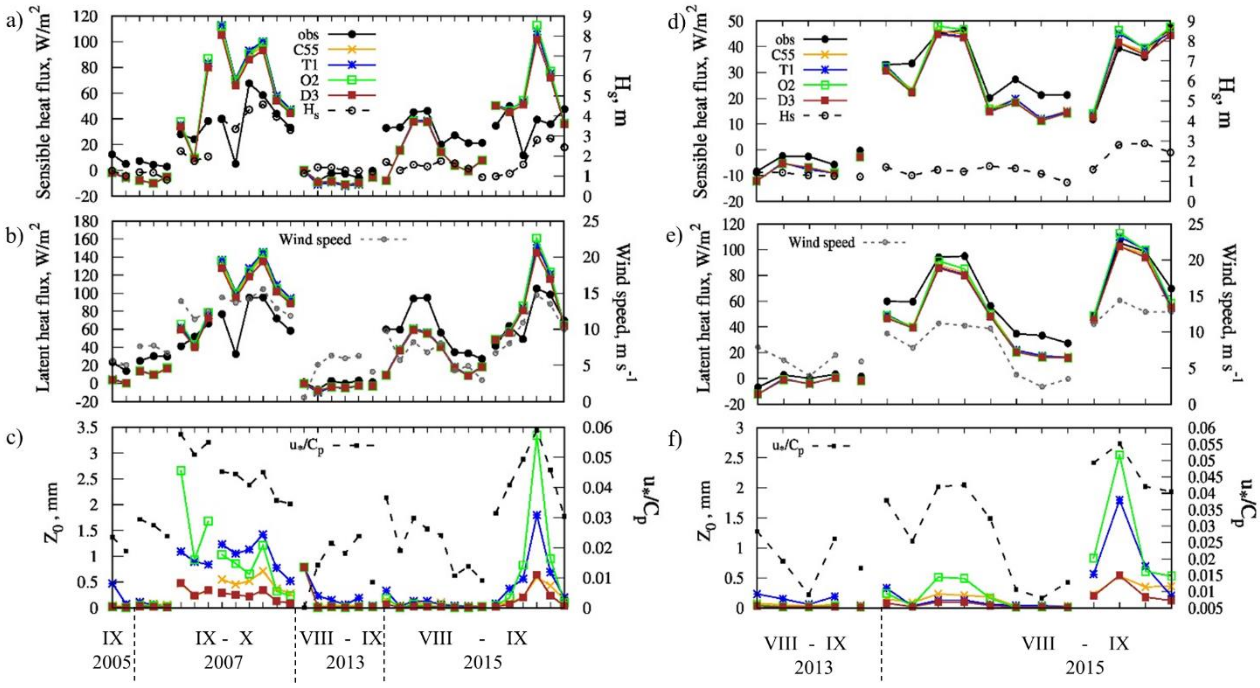

Figure 10. Sensible (a, d) and latent (b, e) heat fluxes and roughness length (c, f) according to NABOS observations (black solid line) and calculated using various roughness parameterizations (color solid lines). Calculations are made on the basis of reanalysis (a-c) and observational data (d-f) (where observations of wind speed, temperature and radiative fluxes are available). Also significant wave height H_s from WWIII simulations (a-d), wind speed from reanalysis (b) and observations (e) and inverse wave age u_*/c_p (c, f) are shown.

The correlation coefficient between the observed and the calculated fluxes from reanalysis data (Figure 10 a,b) is 0.7 for the sensible heat flux and 0.8 for the latent heat flux. However, the mean absolute error (MAE) is rather large - about 20 W m^{-2}. The error magnitude increases with the increase of the heat flux magnitude. The error may be connected both with the COARE algorithm itself and with the input data (i.e., related to the quality of meteorological parameters in the reanalysis). For example, a strong overestimation of heat fluxes on October 11–12, 2007 is associated with the overestimation of wind speed (by 6–8 m s^{-1}) compared to observations.

In order to estimate the accuracy of the COARE algorithm itself and to exclude the reanalysis error, we additionally performed calculations on the basis of shipborne meteorological observations (Figure 10d-f). In these calculations we set precipitation intensity at zero and boundary layer height at 600 m, since these parameters were not observed. The correlation coefficient between the observed and the calculated fluxes from observational data is 0.98-0.99; MAE is reduced to ~ 4 W m^{-2} for sensible heat flux and to ~ 8 W m^{-2} for latent heat flux. This error is within the accuracy of the eddy-covariance method. The accuracy of this method in the case of ship measurements can be significantly reduced due to the influence of air flow distortion by the ship. Therefore, we can conclude that the calculated fluxes are in good agreement with the observations.

Heat fluxes calculated with different roughness parameterizations are almost identical (Figure 10); an average difference between them is 1 W m^{-2}. This difference is maximal in October 2007 and September 2015 (up to 11% of the heat fluxes magnitudes) when inverse wave age (Figure 10c,f) is greater than 0.05, which is a threshold for the young sea. Calculated roughness length (Figure 10c,f) differs by up to 7 times for those cases. However, most cases are characterised by developed sea situation ($u_*/c_p < 0.05$), when all parametrizations should behave well (Drennan et al. 2005). And this must be the reason for small differences in roughness length and heat fluxes. The small difference between parametrizations makes it impossible to unambiguously define the parametrization that fits observations better.

3.4 Long-term mean turbulent heat fluxes

Here we consider the mean long-term values of heat fluxes calculated from the CFSR reanalysis data using COARE algorithm and various roughness parameterizations. The mean long-term (1979-2017) sensible and latent heat flux obtained in the experiment C55 and the differences between experiments shown on Figure 11, 12. The main conclusion of these results is the presence of positive difference for T1 and O2 experiments and negative for D3. The long-term values of difference are small: 1-2 W m^{-2} for T1 and 0.5-1 W m^{-2} for O2.

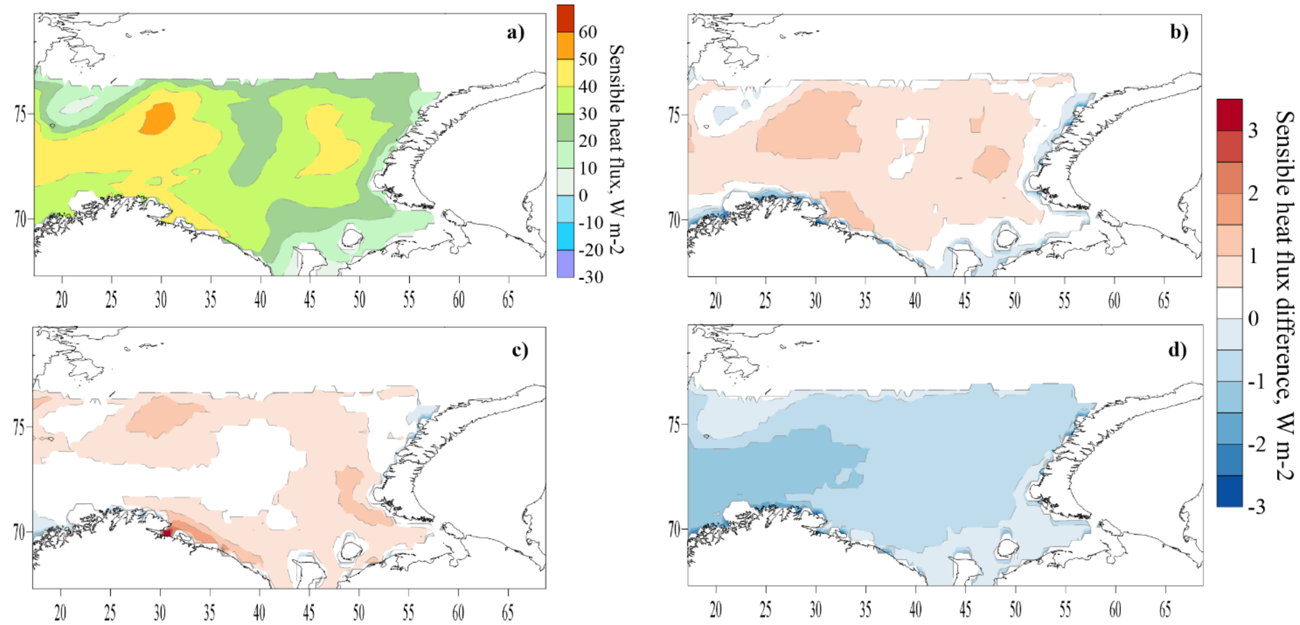

Figure 11. Mean sensible heat flux in the experiment C55 (a,) and the difference in the sensible heat fluxes between experiments T1 - C55 (b), O2 - C55 (c) and D3 - C55 (d). All grid nodes where sea ice was in more than half of the cases are filtered.

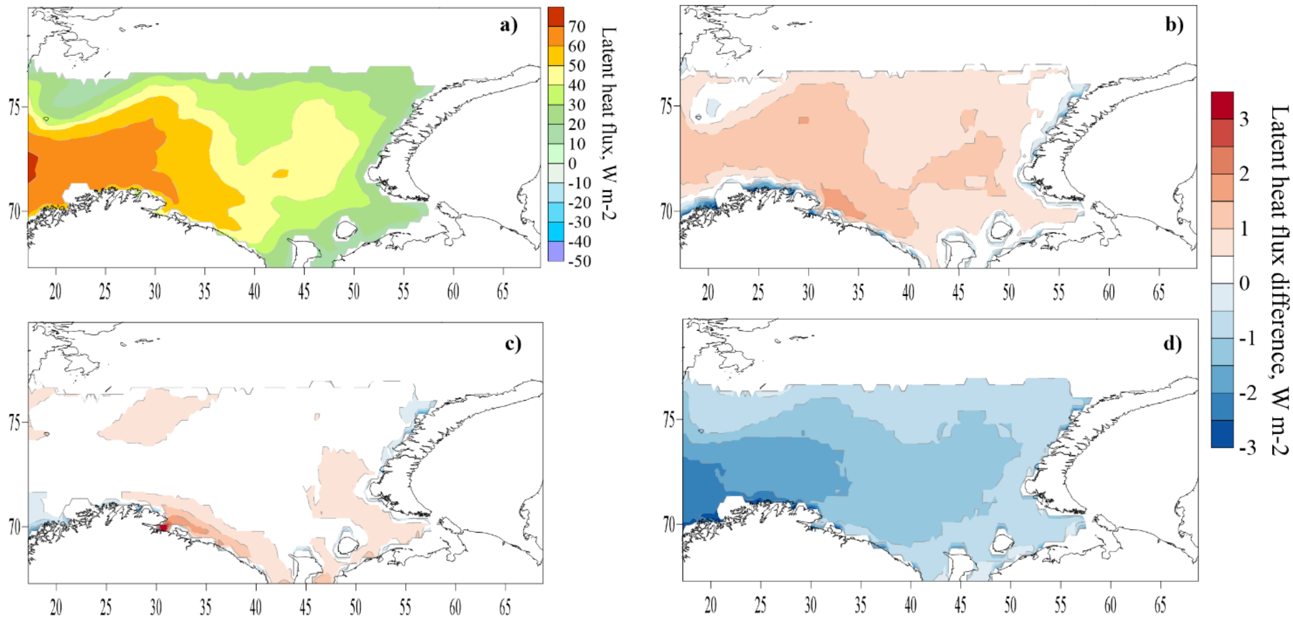

Figure 12. Mean latent heat flux in the experiment C55 (a,) and the difference in the latent heat fluxes between experiments T1 - C55 (b), O2 - C55 (c) and D3 - C55 (d). All grid nodes where sea ice was in more than half of the cases are filtered.

Tables 1, 2 show the average statistics: the difference in heat fluxes with and without explicit accounting for sea waves parameters. Over the entire Barents Sea, the full range of differences in the fluxes are small, within -3 ~ 2 W m^{-2}, which is only 1-3% of the mean absolute value. The greatest mean difference for sensible heat flux observed for T1 and for latent heat flux for O2 parametrization.

The flux difference can exceed 30-50 W m^{-2} (in 0.1% of cases or 99.9 percentile) and in some extreme cases reach 100-250 W m^{-2}. The highest maxima of the flux difference are obtained for the experiment O2.

Table 1

Statistical characteristics of the difference in the sensible heat flux calculated with and without explicit accounting for sea waves parameters: mean difference, relative mean (ratio of the mean difference to the mean value of the flux), mean absolute difference, 95 and 99.9 percentile and the maximum difference for the Barents Sea

	Mean difference (W m^{-2})	Relative mean difference (%)	Mean absolute difference (W m^{-2})	95 percentile (W m^{-2})	99.9 percentile (W m^{-2})
T1 - C55	0.5	1.4	1.7	7.3	40
O2 - C55	0.6	2.1	1.6	6.7	56
D3 - C55	-0.7	-2.3	1.1	3.7	35

Table 2

Statistical characteristics of the difference in the latent heat flux calculated with and without explicit accounting for sea waves: mean, relative mean (ratio of the mean difference to the mean value of the flux), mean absolute difference, 95 and 99.9 percentile and the maximum difference for the Barents Sea

	Mean difference	Relative mean	Mean absolute	95 percentile	99.9 percentile

	($W\ m^{-2}$)	difference (%)	difference ($W\ m^{-2}$)	($W\ m^{-2}$)	($W\ m^{-2}$)
T1 - C55	0.7	1.6	1.8	6.7	41
O2 - C55	0.6	1	1.7	6.4	50
D3 - C55	-1.1	-2.8	1.3	3.7	38

The greatest differences between the experiments are found in those areas where the highest values of the heat fluxes are observed. This can be explained by the power-law dependence of the roughness length on the friction velocity / wave height. Moreover, in the O2 parameterization, the proportionality coefficient is larger (a2 = 4.5) than in the D3 parameterization (a3 = 3.4), which is reflected in the flux differences.

A more detailed spatial analysis of 99.9 percentile of sensible heat flux difference shown on Figure 13. The extreme values of the flux difference taking O2-C55 difference as an example showed that some of the extrema are associated with coastal areas, mainly off the western coast of Novaya Zemlya during bora. Other extremes were associated with deep cyclones in different parts of the sea, with different distances from the coast. Some extremes are associated with storm waves or are observed immediately after storms, during cold-air outbreaks in the rear of cyclones. Therefore, the characteristics of heat fluxes during storm waves and cold-air outbreaks will be considered separately in the following sections.

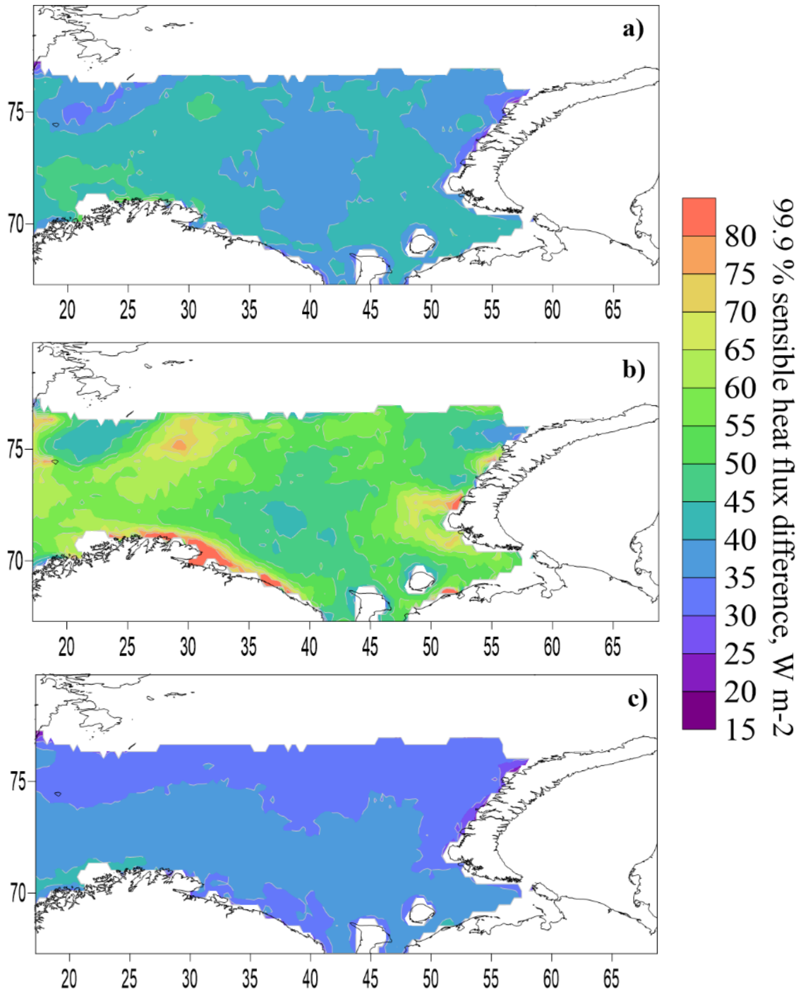

Figure 13. 99.9 percentile of sensible heat flux difference between experiments T1 - C55 (a), O2 - C55 (b) and D3 - C55 (c)

3.5 Turbulent heat fluxes during storm wave events

Here we consider turbulent heat fluxes during the storms identified in Section 3.1 (a total of 1964 days with storms for the period 1979-2017). The spatial distribution of heat fluxes during storms (Figure 14, 15) resembles the average distribution (Figure 11, 12), but the absolute values increase by almost a factor of 2. The average sensible heat flux has several maxima - in the northwest of the sea, near the coast of the Kola Peninsula and a less pronounced local maximum off the southern island of Novaya Zemlya. The flux difference between the experiments is also distributed the same as on average and increases in absolute value (except for experiment D3). The average flux difference between experiments reaches 4-5 W m^{-2} for T1-C55, 8 W m^{-2} for O2-C55 and 3-4 W m^{-2} for D3-C55. On average, the relative difference in heat fluxes is 3% for T1-C55 and 3-5% for O2-C55. The correlation coefficient between the magnitude of the flux and the magnitude of the flux difference is 0.9. For the D3 experiment, the flux difference gradually increases from east to west, and some special structure associated precisely with storms does not appear. The detected maxima of flux difference in the western part of Sea generally correspond to the maxima of the average wave height (Figure 4).

It can be concluded that the mean pattern of heat fluxes in the Barents Sea is largely contributed by storms.

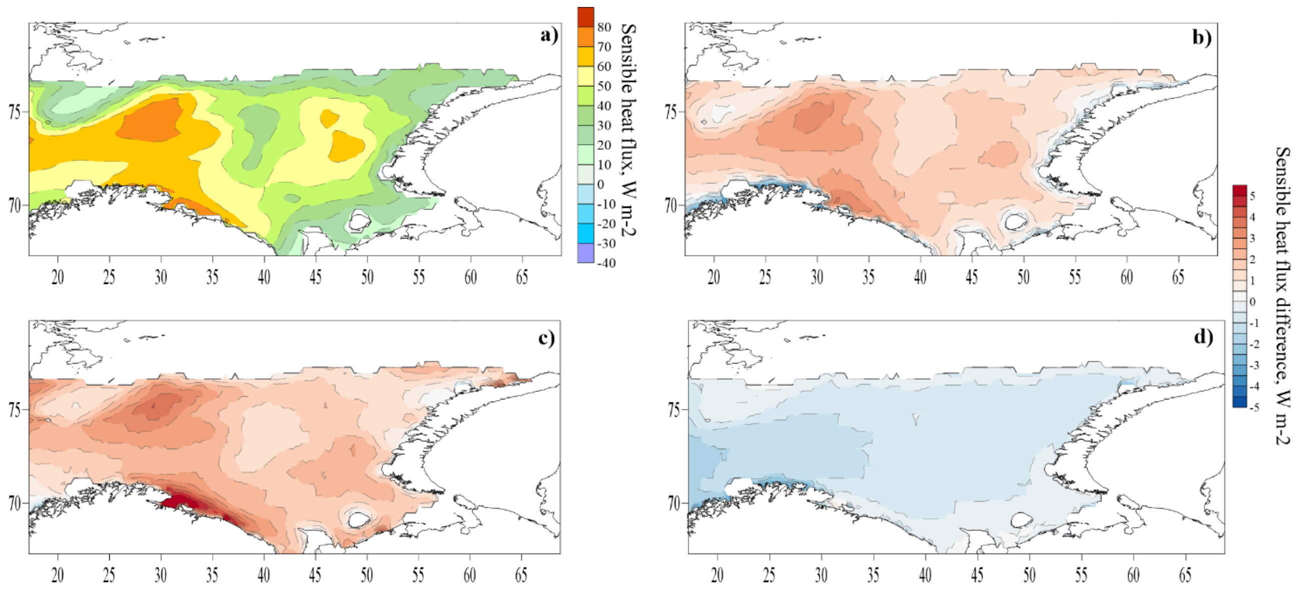

Figure 14. Mean sensible heat flux in experiment C55 (a) and the flux difference in experiments T1 - C55 (b), O2 - C55 (c) and D3 - C55 (d) during storms.

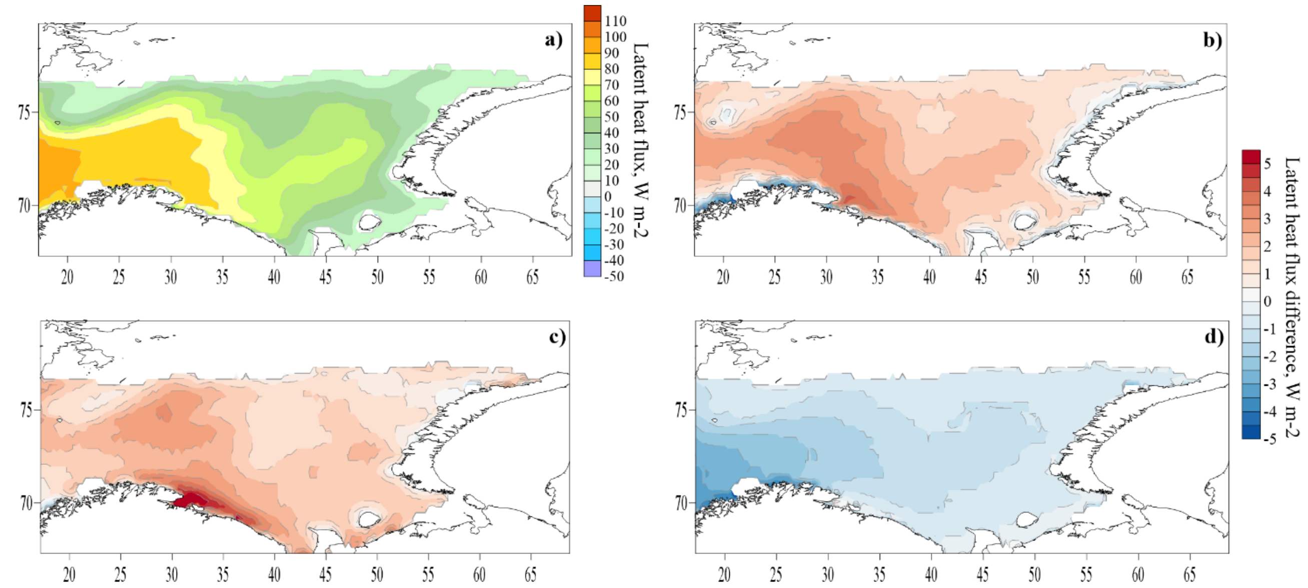

Figure 15. Mean latent heat flux in experiment C55 (a) and the flux difference in experiments T1 - C55 (b), O2 - C55 (c) and D3 - C55 (d) during storms.

3.6 Turbulent heat fluxes during the cold-air outbreaks

Here we consider turbulent heat fluxes during cold-air outbreaks identified in Section 3.2 (2326 days with cold-air outbreaks for the period 1979-2017). The average values of the sensible heat flux increase, especially in the northwestern part (2 times compared with the average), during cold-air outbreaks (Figure 16a). The spatial distribution of the latent heat flux is almost the same with the average one, but the flux magnitude increases by 1.5 times (Figure17a).

Experiments T1 and O2 increase everywhere the magnitude of the sensible and latent heat fluxes compared to C55 during cold-air outbreaks (Figure 16, 17). Explicit accounting for the storm wave events leads to an increase in heat fluxes mainly in the northwest of the sea and near the ice edge. But the differences between the experiments are still small - on average less than 4 W m $^{-2}$ for the sensible heat flux and less than 2.5 W m^{-2} for the latent heat flux, i.e. less than 3-4% of flux magnitudes (Figure 16, 17). At the same time, the extreme values of the flux difference during cold-air outbreaks, as for storm waves, are several times smaller than when considering long-term means.

The average values of the flux difference during cold-air outbreaks are smaller than during storms, but the extreme values during cold-air outbreaks and during storms are close.

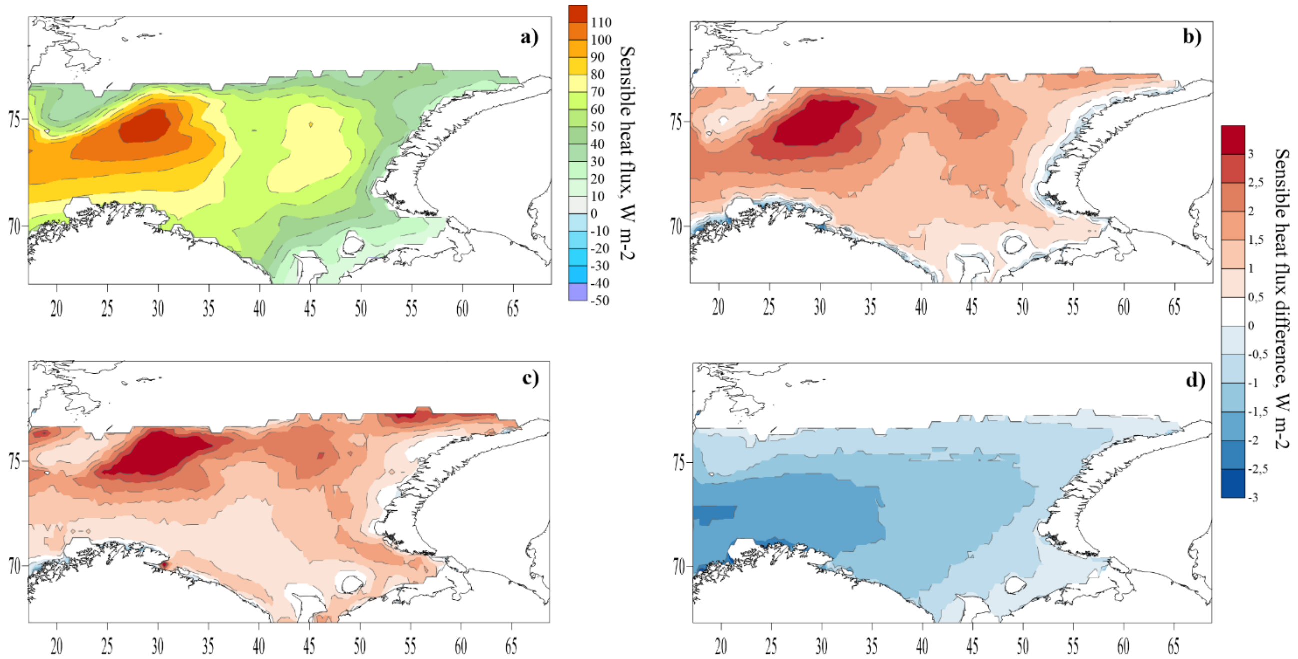

Figure 16. Mean sensible heat flux in experiment C55 (a) and the flux difference in experiments T1 - C55 (b), O2 - C55 (c) and D3 - C55 (d) during cold-air outbreaks.

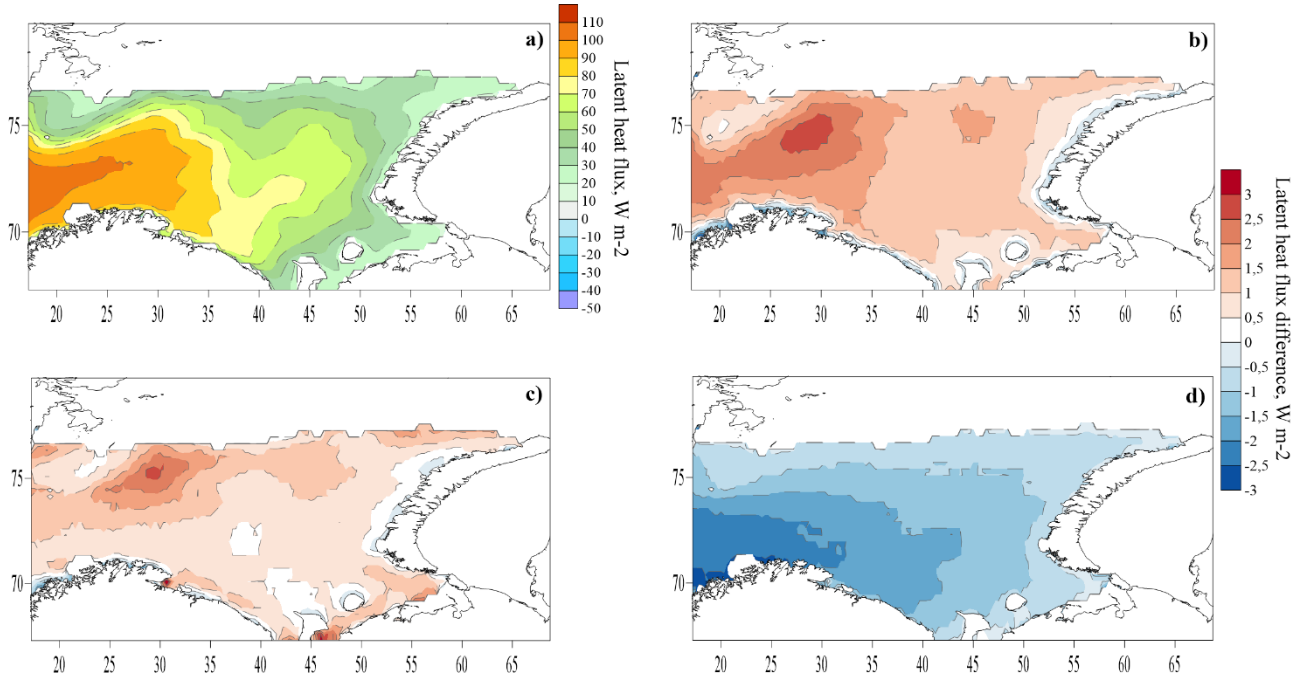

Figure 17. Mean latent heat flux in experiment C55 (a) and the flux difference in experiments T1 - C55 (b), O2 - C55 (c) and D3 - C55 (d) during cold-air outbreaks.

3.7 Turbulent heat fluxes during the simultaneously observed storm waves and cold-air outbreaks

Finally, we consider cases when cold-air outbreaks and storm wave events were simultaneously observed (a total of 292 days for the period 1979-2017) (Figure 18, 19). The magnitude of the heat fluxes and the difference between the experiments in these cases are the largest in comparison with other situations. The sensible heat flux in experiment C55 reaches 170 W m^{-2} (in the north-west of the sea), the latent heat flux is 140 W m^{-2} (in the west). The average difference T1-C55 reaches 6 W m^{-2} for sensible heat flux and 4.5 W m^{-2} for latent heat flux. The average difference O2-C55 reaches 10 W m^{-2} for sensible heat flux and 7 W m^{-2} for latent heat flux. The average difference

D3-C55 reaches 3 W m^{-2} in the west of the sea.

The extreme values of the difference, which can reach 700 W m^{-2}, are also greatest in the case of simultaneously observed storms and cold-air outbreaks. Figure 20 shows case when the difference in sensible heat fluxes exceeded 100 W m^{-2} between C55 and T1 parametrizations and 400 W m^{-2} between C55 and O2 parametrizations. The greatest difference is noted for the eastern local maximum of the heat flux. There, the wind was blowing from the south-east (on the front side of the cyclone) and reached 15-20 m/s; however, wave height and especially wave length were rather low due to short fetch. The storm cyclone was moving very fast over the Barents Sea, which resulted in fast changes of wind direction and velocity in the eastern side of the sea. Thus, it was a very young sea state that resulted in such a difference between parametrizations. An analysis of other cases, in which extreme values of the flux difference were observed, also showed the presence of two local maxima (western and eastern) of heat fluxes. The same maxima also appear in the long-term mean pattern of heat fluxes (Figure 16, 17) and are associated with the cyclone structure and sea ice edge configuration: strong south-easterly winds in front of the cyclone and northerly winds in the rear both produce young waves on short fetches, that contribute much to augmented roughness and heat fluxes.

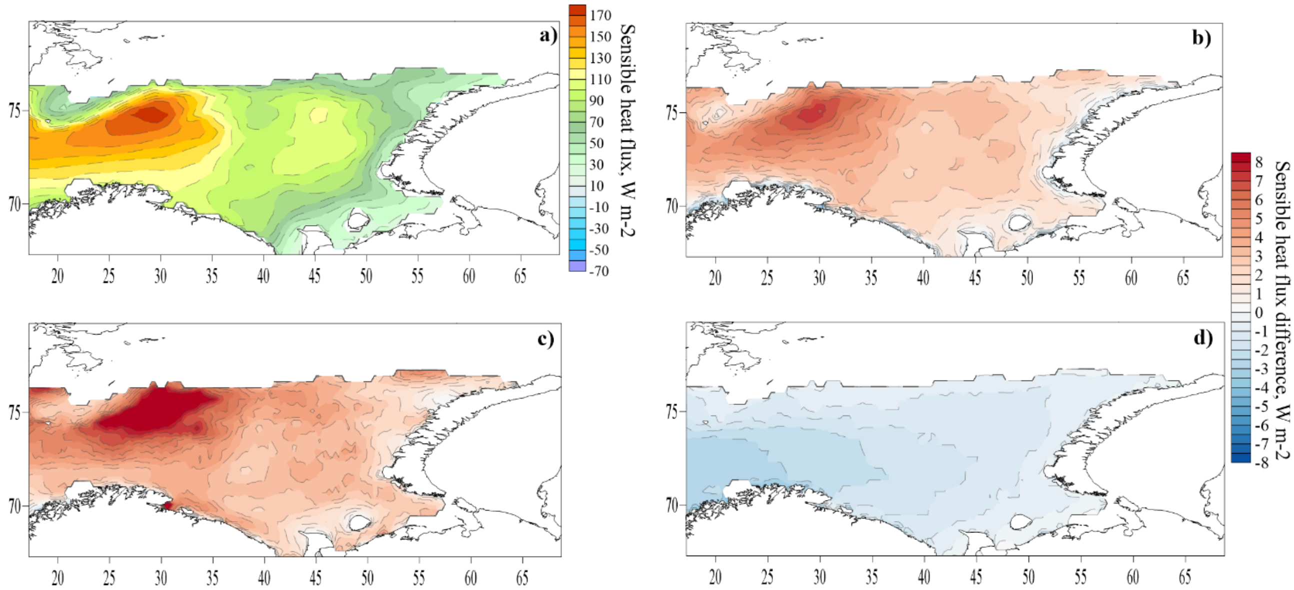

Figure 18. Mean sensible heat flux in experiment C55 (a) and the flux difference in experiments T1 - C55 (b), O2 - C55 (c) and D3 - C55 (d) during storms and cold-air outbreaks.

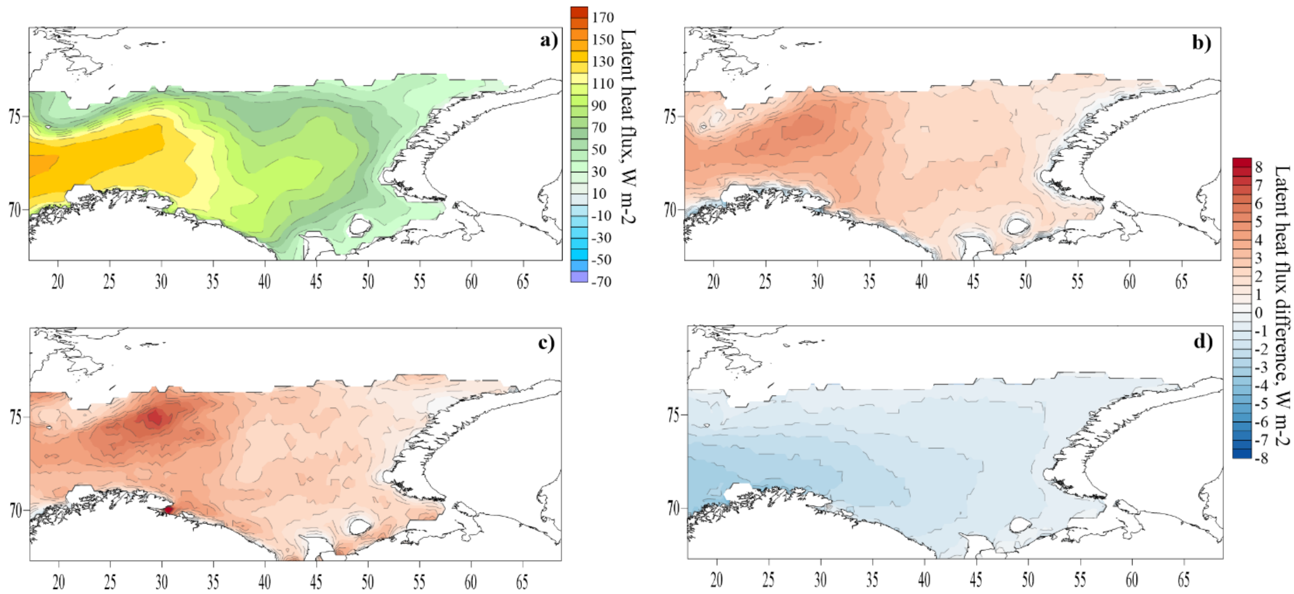

Figure 19. Mean latent heat flux in experiment C55 (a) and the flux difference in experiments T1 - C55 (b), O2 - C55 (c) and D3 - C55 (d) during storm waves and cold-air outbreaks.

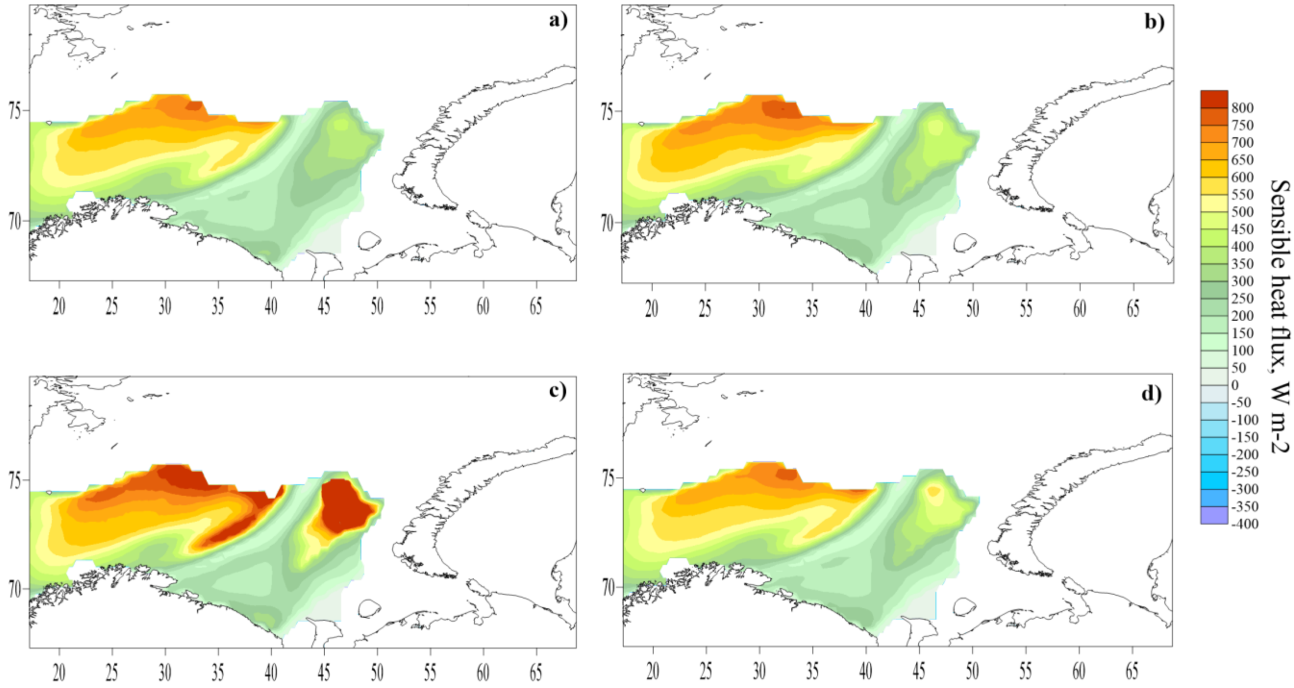

Figure 20. Sensible heat fluxes at 00 UTC January 13, 2003 calculated with C55 (a), T1(b), O2(c) and D3(d) parametrizations.

4. Discussion and conclusions

This paper presents the results of turbulent heat flux calculations in the Barents Sea using the COARE algorithm, meteorological data from reanalysis and sea-wave data from retrospective simulations with the WWIII wave model. The calculations were performed for several options: using the modified Charnock parameterization of roughness length (C55) and using the explicit accounting for the sea waves parameters in the roughness parametrizations T1 (Taylor and Yelland), O2 (Oost et al.) and D3 (Drennan et al.). Particular attention was paid to the episodes with extremely intense energy exchange between the atmosphere and the ocean: storms and cold-air outbreaks (CAOs).

We obtained the mean annual distribution of the height and wavelength in the Barents Sea from wave modelling results. Estimates of the storm activity from 1979 to 2017 were also obtained, confirming its high interannual variability. Based on the data of wave modeling, a catalog of storm waves with the wave height exceeding 5 m was created. This catalog was used to calculate heat fluxes during storms.

The catalog of extreme CAOs over the Barents Sea was also obtained. It is shown that the extreme CAOs are observed in 16.4% of days of a cold season (November-April). However, the number of CAO days varies from 6 in 2011-2012 to 56 in 1981-1982 manifesting large interannual variability. The important role of CAOs in the energy exchange of the Barents Sea and the atmosphere is demonstrated. A high correlation was found between the number of CAO days and turbulent fluxes of sensible and latent heat, as well as with the net flux of long-wave radiation averaged over the ice-free surface of the Barents Sea during a cold season. Thus, the significant interannual variability of the frequency of occurrence of CAOs largely determines the interannual variability of heat loss from the ice-free surface of the Barents Sea.

Comparison of the calculated heat fluxes with ship observations during the NABOS expeditions was carried out. Significant part of the errors in determining the heat fluxes is associated not with the used COARE algorithm, but with discrepancies in meteorological parameters reproduced by the CFSR reanalysis and locally observed on the ship. We estimated the algorithm error as 4 W m^{-2} for sensible heat flux and 8 W m^{-2} for latent heat flux, which is within the accuracy of the eddy-covariance method during ship measurements.

The differences between the experiments (long-term calculations for the period 1979-2017) with different parameterizations of the roughness length are small and are on average 1-3% of the flux magnitude. In some cases, differences can reach 100-200 W m^{-2}. Parameterizations of Taylor and Yelland (2001) and Oost et al. (2002), which represent the dependence of the roughness length on wave steepness and wave length, respectively, on average overestimate the magnitude of the fluxes, and the parameterization of Drennan et al. (2003) (the dependence of the roughness length on wave height and wave age) steadily underestimates the magnitude of the fluxes over the entire sea compared to the Charnock parameterization. Thus, the effect of explicit accounting for wave parameters is small when time averaging is performed and multidirectional, depending on the used parameterization. The modified Charnock formula quite successfully describes the real behavior of the surface roughness even without explicitly taking into account the waves parameters. This can be explained, firstly, by the Charnock parameter dependence on various ranges of wind speed obtained from empirical data, and secondly, by the high correlation between wave parameters and wind speed usually observed. Therefore, in climate studies operating with large time-scales and spatially and temporally averaged values, it can be argued that explicit accounting for sea waves in the calculations of heat fluxes can be neglected.

However, in some situations, the choice of a particular roughness parameterization may be important. During storms and cold-air outbreaks, differences between parameterizations increases along with the turbulent heat transfer increase. In some extreme cases, during storms and cold-air outbreaks, the difference T1-C55 reaches 100 W m^{-2}, the difference O2-C55 exceeded 700 W m^{-2}. O2 parametrization gives the highest values of heat fluxes and roughness length among other parametrizations, and in some cases (in cases of very young sea) calculated values do not correspond to reality. For instance, sensible heat flux reached 1300 W m^{-2} and roughness length reached 7 m in the case, shown on Figure 20. For the same case, roughness length reached only 2 mm in C55 calculations, 1 cm in T1 calculations and 5 cm in D3 calculations. Though D3 parametrization depends on the wave age as well as O2 parametrization, the degree of dependence in the former is lower than in the latter.

The difference between the experiments with parameterization D3 and C55 is almost the same in all cases and always decreases (modulo) from west to east of the sea, actually resembling the mean distribution of wave height. Experiments with parameterizations T1 and O2 deviate most strongly from the Charnok parametrization in those areas and at those times when the absolute values of the fluxes are large. The greatest absolute difference between the fluxes is obtained for the simultaneous action of storms and cold-air outbreaks in the northwest and northeast of the sea, i.e. when the values of the fluxes are the greatest and sea state is young. The relative flux difference (the difference normalized to the value of the flux) over the entire sea is greatest during storms (in some areas more than 5%) (Figure 21), but in some areas (in the north, near the ice edge), the relative difference is higher at the simultaneous action of cold-air outbreaks and storms. In all situations, the relative difference is large in the region of the Pechora Sea due to the low absolute values of the fluxes. An area of low absolute and relative values of the flux difference is located to the north-east from Bear Island.

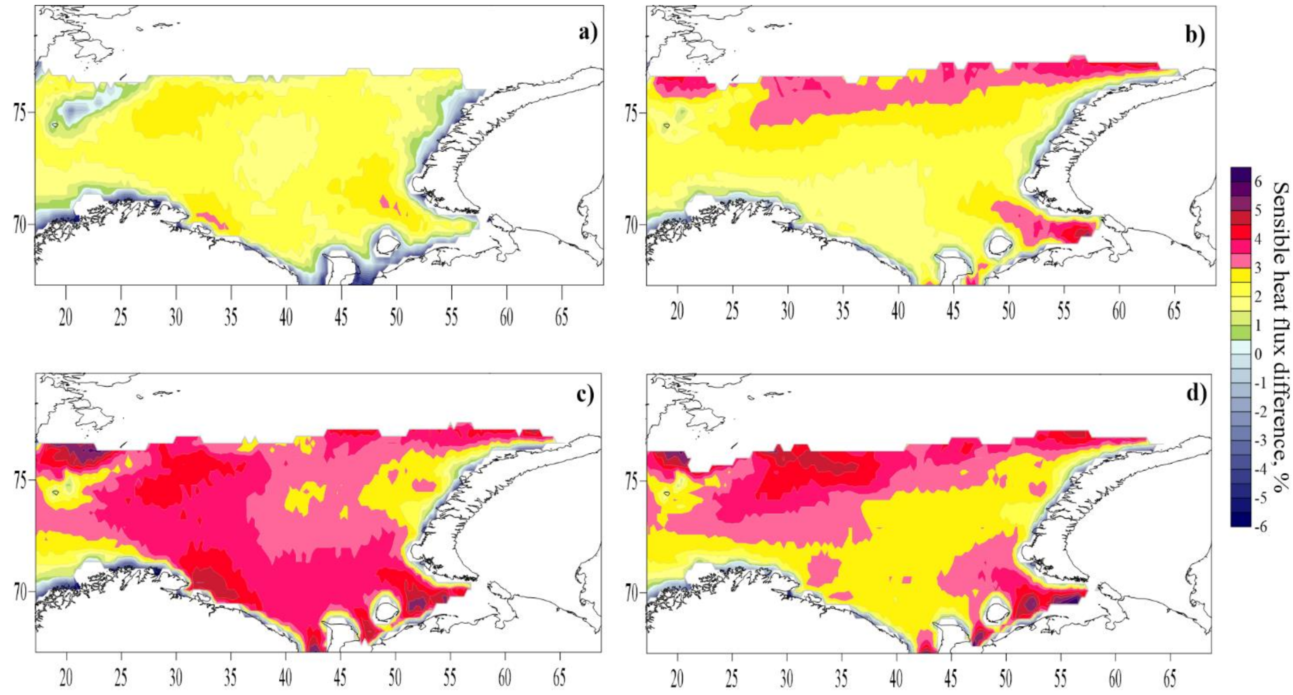

Figure 21. Mean relative difference in sensible heat flux (%) in the experiments T1 - C55 for all cases (a), during cold-air outbreaks (b), during storms (c) and during simultaneously observed storm waves and cold-air outbreaks (d).

Finally, based on the results of our study we can recommend the use of the parametrizations that take into account the wave parameters explicitly on small time scales, for example, in weather prediction, in the Barents Sea region. This is especially true in the case of simultaneous action of storms and cold-air outbreaks, in case of relatively short fetches and young sea state. However, we cannot recommend any particular parametrization due to the lack of in-situ observations in those areas and those times, where heat flux differences in parametrizations are big. Our results highlighted the fact that one should be cautious when using Oost et al. (2002) parametrization in young sea state conditions.

All the conclusions made are valid when turbulent heat fluxes are under consideration. Obviously, differences in the roughness length between calculations with different parametrizations have a more explicit and strong effect on the momentum flux. Although the latter was not the object of this study, nevertheless, its values were estimated as well, and mean relative differences in momentum flux between parametrizations reached 100% of the flux magnitude. Thus, the choice of the parametrization is a key factor in the momentum air-sea exchange applications.

Data availability

Data and results in this article resulting from numerical simulations are available upon request from the corresponding author.

Author contributions

The concept of the study was jointly developed by SM. SM did the numerical simulations, analysis, visualization and manuscript writing. ASh did the Coare simulations and its visualization. DCh did the calculations of cold-air outbreaks repeatability.

Competing interests.

The authors declare that they have no conflict of interest.

Acknowledgments.

Data analysis funded by the RFBR (project 18-05-60083 Shestakova A.A. and Chechin D.G.). The wave modeling was done with the financial support of the RFBR (project 20-35-70039 Myslenkov S.A.). Authors gratefully thank I.A. Repina for the provided shipborne observations collected during NABOS expeditions.

References

Andreas, E. L.: Thermal and size evolution of sea spray droplets (No. CRREL-89-11). Cold Regions Research and Engineering Lab Hanover NH, 1989.

Arthun, M., Schrum, C.: Ocean surface heat flux variability in the Barents Sea. Journal of Marine Systems, 83(1-2), 88-98, https://doi.org/10.1016/j.jmarsys.2010.07.003, 2010.

Barton, B. I., Lenn, Y., & Lique, C.: Observed Atlantification of the Barents Sea Causes the Polar Front to Limit the Expansion of Winter Sea Ice, Journal of Physical Oceanography, 48(8), 1849-1866, 2018.

Beljaars, A. C. M., & Holtslag, A. A. M.: Flux parameterization over land surfaces for atmospheric models. Journal of Applied Meteorology, 30(3), 327-341, https://doi.org/10.1175/1520-0450(1991)030%3C0327:FPOLSF%3E2.0.CO;2, 1991.

Brodeau, L., Barnier, B., Gulev, S. K., & Woods, C.: Climatologically significant effects of some approximations in the bulk parameterizations of turbulent air–sea fluxes. Journal of Physical Oceanography, 47(1), 5-28, https://doi.org/10.1175/JPO-D-16-0169.1, 2017.

Brümmer, B.: Boundary-layer modification in wintertime cold-air outbreaks from the Arctic sea ice. Bound.-Layer Meteor. 80, 109–125, 1996.

Brunke, M. A., Wang, Z., Zeng, X., Bosilovich, M., & Shie, C. L.: An assessment of the uncertainties in ocean surface turbulent fluxes in 11 reanalysis, satellite-derived, and combined global datasets. Journal of Climate, 24(21), 5469-5493, https://doi.org/10.1175/2011JCLI4223.1, 2011.

Brutsaert, W.: Evaporation into the Atmosphere—Theory, History, and Applications. D. Reidel, 299 pp, 1982.

Chechin D.G, Lüpkes C., Repina I.A., Gryanik V.M.: Idealized dry quasi-2D mesoscale simulations of cold-air outbreaks over the marginal sea-ice zone with fine and coarse resolution. J. Geophys. Res., 118, pp. 8787-8813, doi: 10.1002/jgrd.50679, 2013.

Chechin D.G., Zabolotskikh E.V., Repina I.A., Shapron B.: Influence of baroclinicity in the atmospheric boundary layer and Ekman friction on the surface wind speed during cold-air outbreaks in the Arctic, Izv. Atmos. Ocean. Phys., Vol. 51 No. 2, pp. 127–137, doi: 10.1134/S0001433815020048, 2015.

Chechin D.G, Lüpkes C.: Boundary-layer development and low-level baroclinicity during high-latitude cold-air outbreaks: a simple model. Boundary-Layer Meteorol 162: 91. https://doi.org/10.1007/s10546-016-0193-2, 2017.

Chechin, D. G. and Lüpkes, C.: Baroclinic low-level jets in Arctic marine cold-air outbreaks. IOP Conference Series: Earth and Environmental Science, IOP Publishing, 231, 012011, 2019.

Charles, E., Hemer, M.: Parameterization of a wave-dependent surface roughness: A step towards a fully coupled atmosphere-ocean-sea ice-wave system. In 13th International Workshop on Wave Hindcasting and Forecasting and 4th Coastal Hazard Symposium, 2013.

Charnock, H.: Wind stress on a water surface. Quarterly Journal of the Royal Meteorological Society, 81(350), 639-640, 1955.

Drennan, W. M., Graber, H. C., Hauser, D. and Quentin, C.: On the wave age dependence of wind stress over pure wind seas. Journal of Geophysical Research, 108(C3), 8062, 2003.

Drennan, W. M., Taylor, P. K., and Yelland, M. J.: Parameterizing the sea surface roughness. Journal of physical oceanography, 35(5), 835-848, 2005.

ECMWF: Part VII: ECMWF wave model. IFS Documentation Cy31r1, 56 pp. [Available online at http://www.ecmwf.int/research/ifsdocs/CY31r1/WAVES/IFSPart7.pdf.], 2007.

Fairall, C. W., Bradley, E. F., Hare, J. E., Grachev, A. A., & Edson, J. B.: Bulk parameterization of air–sea fluxes: Updates and verification for the COARE algorithm. Journal of climate, 16(4), 571-591, https://doi.org/10.1175/1520-0442(2003)016%3C0571:BPOASF%3E2.0.CO;2, 2003.

Fairall, C. W., Bradley, E. F., Rogers, D. P., Edson, J. B., & Young, G. S.: Bulk parameterization of air-sea fluxes for tropical ocean-global atmosphere coupled-ocean atmosphere response experiment. Journal of Geophysical Research: Oceans, 101(C2), 3747-3764, https://doi.org/10.1029/95JC03205, 1996.

Fletcher, J., S. Mason, and C. Jakob: The Climatology, Meteorology, and Boundary Layer Structure of Marine Cold Air Outbreaks in Both Hemispheres. J. Climate, **29**, 1999–2014, https://doi.org/10.1175/JCLI-D-15-0268.1, https://doi.org/10.1175/JCLI-D-15-0268.1, 2016.

Grachev, A.A., Fairall, C.W. & Bradley, E.F.: Convective Profile Constants Revisited. Boundary-Layer Meteorology 94(3): 495-515, 2000.

Grønas A., Skeie P.: A case study of strong winds at an Arctic front. Tellus 51:865–879, https://doi.org/10.3402/tellusa.v51i5.14498, 1999.

Häkkinen, S., Cavalieri, D. J.: A study of oceanic surface heat fluxes in the Greenland, Norwegian, and Barents Seas. Journal of Geophysical Research: Oceans, 94(C5), 6145-6157, https://doi.org/10.1029/JC094iC05p06145, 1989.

Hasselmann, S., and K. Hasselmann: Computations and parameterizations of the nonlinear energy transfer in a gravity-wave spectrum, Part I: A new method for efficient computations of the exact nonlinear transfer integral. J. Phys. Oceanogr. 15, 1,369–1,377, 2018.

Ivanov, V., Varentsov, M., Matveeva, T., Repina, I., Artamonov, A., & Khavina, E.: Arctic Sea Ice Decline in the 2010s: The Increasing Role of the Ocean—Air Heat Exchange in the Late Summer. Atmosphere, 10(4), 184, 2019.

Ivanov V. V., Timokhov L.A.: Atlantic water in the arctic circulation transpolar system. Russian Meteorology and Hydrology. Vol. 44, no. 4. 238–249, https://doi.org/10.3103/S1068373919040034, 2019.

Janssen, P. A.: Quasi-linear theory of wind-wave generation applied to wave forecasting. Journal of physical oceanography, 21(11), pp. 1631-1642, https://doi.org/10.1175/1520-0485(1991)021%3C1631:QLTOWW%3E2.0.CO;2, 1991.

Jones, I. S., Toba, Y. (Eds.).:Wind stress over the ocean. Cambridge University Press, 2001.

Kaimal, J. C., Wyngaard, J. C., Izumi, Y., and Cote 0. R.: Spectral Characteristics of Surface-Layer Turbulence. Quart. J. Roy. Meteorol. Soc. 98, 563-589, 1972.

Kim, T., Moon, J. H., Kang, K.: Uncertainty and sensitivity of wave-induced sea surface roughness parameterisations for a coupled numerical weather prediction model. Tellus A: Dynamic Meteorology and Oceanography, 70(1), 1-18, https://doi.org/10.1080/16000870.2018.1521242, 2018.

Kolstad E. W., Bracegirdle T.J.: Marine cold-air outbreaks in the future: an assessment of IPCC AR4 model results for the Northern Hemisphere. Clim. Dyn. 30:871–885. doi:10.1007/s00382-007-0331-0, https://doi.org/10.1007/s00382-007-0331-0, 2008.

Kolstad, E.W., Bracegirdle, T.J. and Seierstad, I.A.: Marine cold-air outbreaks in the North Atlantic: temporal distribution and associations with large-scale atmospheric circulation. Clim Dyn 33, 187–197, doi:10.1007/s00382-008-0431-5, 2009.

Kolstad E.W.: Extreme small-scale wind episodes over the Barents Sea: When, where and why? Clim Dyn, 45, 2137-2150, doi:10.1007/s00382-014-2462-4, 2015.

Large W. G. and S. G. Yeager: The global climatology of an interannually varying air-sea flux data set. Climate Dynamics, 33, 341-364 (DOI: 10.1007/s00382-008-0441-3), 2009.

Li Jingkai, Ma Y, Liu Q, Zhang W and Guan C: Growth of wave height with retreating ice cover in the Arctic. Cold Regions Science and Technology, 164, 102790. doi: 10.1016/j.coldregions.2019.102790, 2019.

Liu, W. T., Katsaros, K. B., & Businger, J. A.: Bulk parameterization of air-sea exchanges of heat and water vapor including the molecular constraints at the interface. Journal of the Atmospheric Sciences, 36(9), 1722-1735, 1979.

Liu Q., Babanin A., Zieger S., Young I., Guan C.: Wind and wave climate in the Arctic Ocean as observed by altimeters. J. Climate. 2016. V. 29(22). P. 7957–7975, https://doi.org/10.1175/JCLI-D-16-0219.1, 2016.

Mahrt, L., Vickers, D., Frederickson, P., Davidson, K., & Smedman, A. S.: Sea-surface aerodynamic roughness. Journal of Geophysical Research: Oceans, 108(C6), https://doi.org/10.1029/2002JC001383, 2003.

Moore G.W.K.: The Novaya Zemlya Bora and its impact on Barents Sea air-sea interaction, Geophys. Res. Lett., 40, 3462 — 3467, doi:10.1002/grl.50641, 2013.

Myslenkov S., Medvedeva A., Arkhipkin V., Markina M., Surkova G., Krylov A., Dobrolyubov S., Zilitinkevich S., Koltermann P.: Long-term statistics of storms in the Baltic, Barents and White Seas and their future climate projections. Geography, Environment, Sustainability.V. 11. № 1. P. 93–112, https://doi.org/10.24057/2071-9388-2018-11-1-93-112, 2018.

Myslenkov S.A., Arkhipkin V.S., Koltermann K.P.: Evaluation of swell height in the Barents and White Seas, Moscow University Bulletin, Series 5. Geography. №5, pp.59-66, 2015.

Myslenkov, S.A., Markina, M.Yu., Arkhipkin, V.S., Tilinina, N.D.: Frequency of storms in the Barents sea under modern climate conditions. Vestnik Moskovskogo Universiteta, Seriya 5: Geografiya. Volume, Issue 2, 2019, Pages 45-54, 2019.

Myslenkov S.A., Markina M. Yu., Kiseleva S.V. et al.: Estimation of Available Wave Energy in the Barents Sea. Thermal Engineering. 65, 7, 411–419, https://doi.org/10.1134/S0040601518070054, 2018.

Narizhnaya A.I., Chernokulsky A.V., Akperov M.G., Chechin D.G., Esau I., Timazhev A.V.: Marine cold air outbreaks in the Russian Arctic: climatology, interannual variability, dependence on sea-ice concentration. IOP Conf. Ser.: Earth Environ. Sci. 606 012039, https://doi.org/10.1088/1755-1315/606/1/012039, 2020.

Oost, W. A., Komen, G. J., Jacobs, C. M. J., & Van Oort, C.: New evidence for a relation between wind stress and wave age from measurements during ASGAMAGE. Boundary-Layer Meteorology, 103(3), 409-438, 2002.

Pan, Y., Sha, W., Zhu, S., Ge, S.: A new parameterization scheme for sea surface aerodynamic roughness. Progress in Natural Science, 18(11), 1365-1373, https://doi.org/10.1023/A:1014913624535, 2008.

Papritz, L. and T. Spengler: A Lagrangian Climatology of Wintertime Cold Air Outbreaks in the Irminger and Nordic Seas and Their Role in Shaping Air–Sea Heat Fluxes. J. Climate, 30, 2717–2737, https://doi.org/10.1175/JCLI-D-16-0605.1, 2017.

Papritz, L. and Grams, C. M.: Linking low-frequency large-scale circulation patterns to cold air outbreak formation in the north- eastern North Atlantic. Geophysical Research Letters, 45, 2542–2553. https://doi.org/10.1002/2017GL076921, 2018.

Pithan, F. , Svensson, G. , Caballero, R. , Chechin, D. , Cronin, T. W. , Ekman, A. M. L. , Neggers, R. , Shupe, M. D. , Solomon, A. , Tjernström, M. and Wendisch, M.: Role of air-mass transformations in exchange between the Arctic and mid-latitudes , Nature Geoscience, 11 (11), pp. 805-812, https://doi.org/10.1038/s41561-018-0234-1, 2018.

Pope, J.O., Bracegirdle, T.J., Renfrew, I.A. et al.: The impact of wintertime sea-ice anomalies on high surface heat flux events in the Iceland and Greenland Seas. Clim Dyn 54, 1937–1952. https://doi.org/10.1007/s00382-019-05095-3, 2020.

Prakash, K. R., Pant, V., Nigam, T.: Effects of the Sea Surface Roughness and Sea Spray-Induced Flux Parameterization on the Simulations of a Tropical Cyclone. Journal of Geophysical Research: Atmospheres, 124(24), https://doi.org/10.1029/2018JD029760, 2019.

Rahmstorf, S., Ganopolski, A.: Long-Term Global Warming Scenarios Computed with an Efficient Coupled Climate Model. Climatic Change 43, 353–367. https://doi.org/10.1023/A:1005474526406, 1999.

Renfrew, I. A., Moore, G. K., Guest, P. S., & Bumke, K.: A comparison of surface layer and surface turbulent flux observations over the Labrador Sea with ECMWF analyses and NCEP reanalyses. Journal of Physical Oceanography, 32(2), 383-400, https://doi.org/10.1175/1520-0485(2002)032%3C0383:ACOSLA%3E2.0.CO;2, 2002.

Ribal, A., Young, I.R.: 33 years of globally calibrated wave height and wind speed data based on altimeter observations. Sci Data 6, 77. https://doi.org/10.1038/s41597-019-0083-9, 2019.

Saha S. et al.: The NCEP climate forecast system reanalysis. Bul. of the American Meteorological Society. V. 91. № 8. P. 1015–1057, https://doi.org/10.1175/2010BAMS3001.1, 2010.

Saha S. et al.: The NCEP Climate Forecast System Version 2. J. Climate. 27, 2185—2208, https://doi.org/10.1175/JCLI-D-12-00823.1, 2014.

Savijärvi H. I.: Cold air outbreaks over high-latitude sea gulfs, Tellus A: Dynamic Meteorology and Oceanography, 64:1, DOI: 10.3402/tellusa.v64i0.12244, 2012.

Semedo A, Sušelj K, Rutgersson A, Sterl A.: A global view on the wind sea and swell climate and variability from ERA-40. J Clim 24(5):1461–1479, https://doi.org/10.1175/2010JCLI3718.1, 2011.

Shimura, T., Mori, N., Takemi, T., Mizuta, R.: Long-term impacts of ocean wave-dependent roughness on global climate systems. Journal of Geophysical Research: Oceans, 122(3), 1995-2011, https://doi.org/10.1002/2016JC012621, 2017.

Simonsen, K., Haugan, P. M.: Heat budgets of the Arctic Mediterranean and sea surface heat flux parameterizations for the Nordic Seas. Journal of Geophysical Research: Oceans, 101(C3), 6553-6576, https://doi.org/10.1029/95JC03305, 1996.

Skeie P.: Meridional flow variability over the Nordic Seas in the Arctic Oscillation framework. Geophys. Res. Lett. 27:2569-2572. https://doi.org/10.1029/2000GL011529, 2000.

Smedsrud, L. H., et al.: The role of the Barents Sea in the Arctic climate system, Rev. Geophys., 51, 415–449, doi:10.1002/rog.20017, 2013.

Smith, S. D.: Coefficients for sea surface wind stress, heat flux, and wind profiles as a function of wind speed and temperature. Journal of Geophysical Research: Oceans, 93(C12), 15467-15472, 1988.

Stopa J., Ardhuin F.,Girard-Ardhuin F.: Wave climate in the Arctic 1992-2014: seasonality and trends. Cryosphere, 10(4), pp.1605-1629, https://doi.org/10.5194/tc-10-1605-2016, 2016.

Taylor, P. K., & Yelland, M. J.: The dependence of sea surface roughness on the height and steepness of the waves. Journal of physical oceanography, 31(2), 572-590, https://doi.org/10.1175/1520-0485(2001)031%3C0572:TDOSSR%3E2.0.CO;2, 2001.

Tolman, H.: The WAVEWATCH III Development Group User Manual and System Documentation of WAVEWATCH III version 4.18. Tech. Note 316, NOAA/NWS/NCEP/MMAB, 2014, available at: http://polar.ncep.noaa.gov/waves/wavewatch/ manual.v4.18.pdf (last access: 23 June 2018), 2014.

Varentsov, M.I., Repina, I.A., Artamonov, A. Yu., Khavina, E.M., & Matveeva, T.A.: Experimental studies of energy transfer and the dynamics of the atmospheric boundary layer in the Arctic in the summer. Proceedings of the Hydrometeorological Research Center of the Russian Federation, (361), 95-127, 2016.

Wheeler, D. D., Harvey, V. L., Atkinson, D. E., Collins, R. L., and Mills, M. J.: A climatology of cold air outbreaks over North America: WACCM and ERA-40 comparison and analysis, J. Geophys. Res., 116, D12107, doi:10.1029/2011JD015711, 2011.

Wind and Wave Climate Handbook. Barents, Okhotsk, and Caspian Seas: Ed. by L. I. Lopatukhin, et al. (Russian Maritime. Register Shipping., St. Petersburg, 2003), 2003.

Wu, B., J. Wang, and J.E. Walsh: Dipole Anomaly in the Winter Arctic Atmosphere and Its Association with Sea Ice Motion. J. Climate, 19, 210–225, https://doi.org/10.1175/JCLI3619.1, 2006.

Yu, L., & Jin, X.: Satellite-based global ocean vector wind analysis by the Objectively Analyzed Air-sea Fluxes (OAFlux) Project: Establishing consistent vector wind time series from July 1987 onward through synergizing microwave radiometers and scatterometers (Vol. 1). WHOI OAFlux Tech. Rep. WHOI-OA-2011, 2011.

Zilitinkevich S.S., Grachev A.A., Fairall C.W.: Scaling reasoning and field data on the sea surface roughness lengths for scalars. J. Atmos. Sci. V. 58. P. 320–325, 2001.